The CRISPR Journal
Volume 6, Number 6, 2023

DOI: 10.1089/crispr.2023.0022

The CRISPR Journal

RESEARCH ARTICLE

Differential Divalent Metal Binding by SpyCas9's RuvC Active Site Contributes to Nonspecific DNA Cleavage

Sydney N. Newsom,[1,†] Duen-Shian Wang,[2,†] Saadi Rostami,[1] Isabelle Schuster,[3] Hari Priya Parameshwaran,[1] Yadin G. Joseph,[1] Peter Z. Qin,[3] Jin Liu,[2,*] and Rakhi Rajan[1,*]

Abstract

To protect against mobile genetic elements (MGEs), some bacteria and archaea have clustered regularly interspaced short palindromic repeats-CRISPR associated (CRISPR-Cas) adaptive immune systems. CRISPR RNAs (crRNAs) bound to Cas nucleases hybridize to MGEs based on sequence complementarity to guide the nucleases to cleave the MGEs. This programmable DNA cleavage has been harnessed for gene editing. Safety concerns include off-target and guide RNA (gRNA)-free DNA cleavages, both of which are observed in the Cas nuclease commonly used for gene editing, *Streptococcus pyogenes* Cas9 (SpyCas9). We developed a SpyCas9 variant (SpyCas9^{H982A}) devoid of gRNA-free DNA cleavage activity that is more selective for on-target cleavage. The H982A substitution in the metal-dependent RuvC active site reduces Mn^{2+}-dependent gRNA-free DNA cleavage by ~167-fold. Mechanistic molecular dynamics analysis shows that Mn^{2+}, but not Mg^{2+}, produces a gRNA-free DNA cleavage competent state that is disrupted by the H982A substitution. Our study demonstrates the feasibility of modulating cation:protein interactions to engineer safer gene editing tools.

Introduction

CRISPR-Cas (clustered regularly interspaced short palindromic repeats-CRISPR associated) systems are RNA-directed adaptive immune systems present in bacteria and archaea.[1–3] The CRISPR locus retains immunological memory of past mobile genetic element (MGE) infections as short pieces of intruder genome that are transcribed into CRISPR RNA (crRNA). The crRNA assembles with Cas proteins and the RNA-protein complex is guided, sequence-specifically, to the invading genome for cleavage and inactivation upon subsequent attacks. The sequence-specificity is established by the complementarity between the guide region of the crRNA and the invading DNA or RNA. CRISPR systems possess inherent mechanisms, such as the protospacer adjacent motif (PAM) or the protospacer-flanking site (PFS) to differentiate self and invading nucleic acid.[4] The crRNA-dependent nucleic acid targeting and cleavage features of Cas proteins have been repurposed into powerful genome and biotechnological applications.[5]

Of the numerous CRISPR systems,[6] Cas9, the signature protein of type II CRISPR-Cas systems, is being widely used for gene editing and gene therapy applications due to the simplistic requirements of a single multidomain Cas9 protein and a single-guide RNA (sgRNA, fusion of crRNA, and *trans*-activating crRNA [tracrRNA]) for sequence-specific DNA cleavage.[7] Cas9 uses HNH and RuvC endonuclease domains, respectively, to cleave the complementary strand (target strand DNA, TS-DNA) and noncomplementary strand (nontarget strand DNA, NTS-DNA) of a double-stranded DNA (dsDNA).[7,8]

One of the hallmarks of Cas9's DNA cleavage is the intricate and orchestrated changes in conformation of the different domains of Cas9, sgRNA, and the DNA to establish site-specific DNA cleavage.[9] Cas9 has a bilobed architecture consisting of a recognition (REC) lobe and a nuclease (NUC) lobe, which is connected by an arginine-rich bridge helix.[8,10] The apo-Cas9 crystal structure shows a self-inhibitory form of the protein where the

[1]*Department of Chemistry and Biochemistry, Price Family Foundation Institute of Structural Biology, Stephenson Life Sciences Research Center, The University of Oklahoma, Norman, Oklahoma, USA;* [2]*Department of Pharmaceutical Sciences, University of North Texas System College of Pharmacy, University of North Texas Health Science Center, Fort Worth, Texas, USA; and* [3]*Department of Chemistry, University of Southern California, Los Angeles, California, USA.*
[†]*Both these authors contributed equally to this work.*

*Address correspondence to: *Rakhi Rajan, Department of Chemistry and Biochemistry, Price Family Foundation Institute of Structural Biology, Stephenson Life Sciences Research Center, University of Oklahoma, 101 Stephenson Parkway, Norman, OK 73019, USA,* E-mail: r-rajan@ou.edu; *Jin Liu, Department of Pharmaceutical Sciences, University of North Texas System College of Pharmacy, University of North Texas Health Science Center, 3500 Camp Bowie Blvd, Fort Worth, TX 76107, USA,* E-mail: jin.liu@unthsc.edu.

endonuclease domains are not easily accessible for DNA cleavage,[10] even though studies have shown that Cas9 can bind nonspecifically to DNA in the absence of sgRNA.[11]

Formation of binary (Cas9-sgRNA) and ternary (Cas9-sgRNA-DNA) complexes are tightly regulated by orchestrated protein domain movements.[8–10,12,13] To ensure sequence-specificity of DNA cleavage, the conformational transitions of HNH and RuvC are regulated by RNA:DNA base pairing at the PAM-distal end of the R-loop.[14,15] Even though RuvC is conformationally dependent on the HNH transition to access the scissile phosphates,[12,14] DNA cleavage occurs in a concerted manner.[16–18] Molecular dynamic (MD) simulations have revealed that several allosteric mechanisms mediated by different domains of Cas9, PAM-identification, and DNA binding are essential for DNA cleavage.[18–24]

In spite of the intricate conformational changes essential for sequence-specific DNA cleavage, we previously showed that Cas proteins can promote promiscuous DNA cleavage when cognate guide-RNA is absent.[25] This activity, called guide RNA (gRNA)-free (also known as RNA-independent and guide-free) DNA cleavage[25,26] manifests differently in different Cas endonucleases, is PAM independent, and requires specific divalent metals (such as Mn^{2+} or Co^{2+}) under *in vitro* conditions. *Streptococcus pyogenes* (Spy) Cas9 demonstrated robust degradation of single-stranded circular plasmid in a gRNA-free manner, using its RuvC domain.[25] The presence of even one of the cognate RNAs (crRNA or tracrRNA) does not abolish SpyCas9's gRNA-free DNA cleavage activity.[25]

Other studies have reported effects of gRNA-free DNA cleavage. It was shown that several Cas12a orthologs possess gRNA-free single and dsDNA cleavage activities with diverse divalent cations, including Mg^{2+} ions.[27] SpyCas9 and *Campylobacter jejuni* Cas9 (CjeCas9) were shown to promote gRNA-free DNA cleavage under cellular conditions in human cells, resulting in induction of p53 and γ-H2AX DNA damage markers.[26] This study establishes that cellular conditions (both divalent metal concentrations and forms of DNA) can promote gRNA-free DNA cleavage activity.[26] Studies have also indicated that Cas9 is a virulence factor in *C. jejuni*, where it acts as a cytotoxic agent that is essential for a successful infection of human tissue.[28] These studies show the ability of Cas9 to cleave DNA promiscuously and the ability of the RuvC domain of Cas9 to attain a DNA cleavage competent state in the absence of large conformational rearrangements enabled by RNA and DNA binding. Such promiscuous DNA cleavages can potentially reduce the fidelity of genome applications.

We focused on Cas9's RuvC domain to identify residues that have differential effects toward gRNA-dependent and gRNA-free DNA cleavages. We identified that the H982 residue plays a critical role in promoting gRNA-free DNA cleavage and that it only has a supporting role in catalyzing gRNA-dependent DNA cleavage. The substitution of His982 to Ala ($SpyCas9^{H982A}$) causes ~167-fold reduction in Mn^{2+}-mediated gRNA-free DNA cleavage and the variant adapts a modified mechanism to maintain efficient gRNA-dependent DNA cleavage. Previous studies have shown that H982A substitution lowers off-target DNA cleavage,[29,30] implicating that this substitution can reduce unwarranted genome changes from both off-target and gRNA-free DNA cleavages. MD simulations show that H982 contributes to maintaining the Mn^{2+}_A-Asp10 (RuvC's catalytic residue) interaction at a distance that enables DNA scission in the absence of sgRNA. Protein engineering to remove gRNA-free DNA cleavage will further improve the safety of SpyCas9-based genome tools.

Materials and Methods

Protein purification

Site-directed mutagenesis (SDM) (see Supplementary Table S1 in the Supplementary Information for primer sequences) was used to introduce the H982A substitution ($SpyCas9^{H982A}$) using the Addgene plasmid PMJ806.[7] We used previously established protocols to purify wild-type SpyCas9 ($SpyCas9^{WT}$) and $SpyCas9^{H982A}$.[7,25] Briefly, Rosetta (DE3) cells were grown in 2XYT medium until optical density at 600 nm reached 0.8 and then were induced with 0.2 mM Isopropyl-ß-D-thiogalactopyranoside (IPTG) overnight at 18°C. Cas9 was purified over three columns consisting of Nickel nitrilotriacetic acid (Ni-NTA), cation exchange (SP HP), and size exclusion chromatography (S-300). The final pure fractions were concentrated and the protein aliquots were stored at −80°C (Supplementary Information).[7,25]

Production of sgRNA and plasmid substrate for gRNA-dependent DNA cleavage assays

In vitro run-off transcription and annealing of sgRNA (sequence in Supplementary Table S1 in the Supplementary Information) for gRNA-dependent DNA cleavage assays were performed as previously described.[31] Plasmids containing matched and mismatched target sequences were from a previous study.[31] Supercoiled bands were extracted out of an agarose gel using a kit (QIAquick Gel Extraction Kit; Qiagen, Hilden, Germany) for use as the substrate.

In vitro SpyCas9 activity assays

Detailed methods are described in the Supplementary Materials and Method in the Supplementary Information. Unless otherwise stated, the gRNA-free DNA cleavage reactions contained 1×buffer (20 mM HEPES pH 7.5, 150 mM KCl, 2 mM TCEP), 100 ng (~4.5 nM) single-stranded plasmid DNA (M13mp18, NEB, N4040S), 10 mM divalent metal, and 100 nM SpyCas9. The gRNA-dependent dsDNA cleavage reaction contained 1×cleavage buffer (20 mM Tris pH 7.5, 100 mM KCl, 5% [v/v] glycerol and 0.5 mM TCEP), 100 ng (~5 nM) double-stranded plasmid DNA (pUC19) containing a target site complementary to the guide region of the sgRNA (for time-course assays) or with some mismatches (MM) to the guide region (for off-target DNA cleavage assays), 10 mM divalent metal, 120 nM sgRNA, and 100 nM SpyCas9. For mismatch analysis, we used pUC19 plasmids holding MM at position 3, 5, and 18 with respect to PAM following our previous protocols.[18]

Quantification of DNA cleavage

gRNA-free DNA cleavage of single-stranded plasmids. The agarose gel images were analyzed using ImageJ software[32] to measure the band intensities of the substrate, which included both the circular and linear forms of M13mp18. For each lane, the remaining intensity of substrate (C) was normalized to that of the no-protein control lane (C_0) to obtain the fraction of DNA precursor remaining ($P_{M13mp18}$).

$$P_{M13mp18} = \frac{C}{C_0} \tag{1a}$$

Three replications were averaged, and the program MATLAB (Natick, MA) was used to fit the following one-exponential decay equation to calculate the rate constant for gRNA-free DNA degradation:

$$P_{M13mp18} = e^{-k_{obs}t} \tag{1b}$$

where t is time (min), and k_{obs} is the observed DNA degradation rate constant (min^{-1}).

gRNA-dependent DNA cleavage of supercoiled plasmids. gRNA-dependent activities were characterized using supercoiled plasmid DNA substrates as previously reported.[18] Briefly, cleavage reaction time-points were run on agarose gels to resolve the supercoiled, nicked, and linear DNAs. The normalized fractions of supercoiled precursor (P), nicked intermediate (N), and linear (L) at each time-point were computed as described; then fit globally using a custom-built MATLAB program.[33] Fitting followed a parallel-sequential model as represented by Equations (2)–(4):

$$P = 1 - \alpha \cdot \left[1 - e^{-(k_{1,HNH} + k_{1,RuvC})\cdot t}\right] \tag{2}$$

$$N = N_{TS} + N_{NTS} \tag{3}$$

$$N_{TS} = \alpha \cdot \left\{\frac{k_{1,HNH}}{(k_{1,HNH} + k_{1,RuvC}) - k_{2,RuvC}} \cdot \left[e^{-k_{2,RuvC}\cdot t} - e^{-(k_{1,HNH} + k_{1,RuvC})\cdot t}\right]\right\} \tag{3a}$$

$$N_{NTS} = \alpha \cdot \left\{\frac{k_{1,RuvC}}{(k_{1,HNH} + k_{1,RuvC}) - k_{2,HNH}} \cdot \left[e^{-k_{2,HNH}\cdot t} - e^{-(k_{1,HNH} + k_{1,RuvC})\cdot t}\right]\right\} \tag{3b}$$

$$L = L_{TS,NTS} + L_{NTS,TS} \tag{4}$$

$$L_{TS,NTS} = \alpha \cdot \left[\frac{k_{1,HNH}}{k_{1,HNH} + k_{1,RuvC}} - \frac{k_{1,HNH}}{(k_{1,HNH} + k_{1,RuvC}) - k_{2,RuvC}} \cdot e^{-k_{2,RuvC}\cdot t} + \frac{k_{1,HNH}\cdot k_{2,RuvC}}{(k_{1,HNH} + k_{1,RuvC} - k_{2,RuvC})\cdot(k_{1,HNH} + k_{1,RuvC})} \cdot e^{-(k_{1,HNH} + k_{1,RuvC})\cdot t}\right] \tag{4a}$$

$$L_{NTS,TS} = \alpha \cdot \left[\frac{k_{1,RuvC}}{k_{1,HNH} + k_{1,RuvC}} - \frac{k_{1,RuvC}}{(k_{1,HNH} + k_{1,RuvC}) - k_{2,HNH}} \cdot e^{-k_{2,HNH}\cdot t} + \frac{k_{1,RuvC}\cdot k_{2,HNH}}{(k_{1,HNH} + k_{1,RuvC} - k_{2,HNH})\cdot(k_{1,HNH} + k_{1,RuvC})} \cdot e^{-(k_{1,HNH} + k_{1,RuvC})\cdot t}\right] \tag{4b}$$

with P: fraction of supercoiled precursor; N: fraction of the total nicked product; N_{TS}: fraction of product with only the target-strand (TS) nicked; N_{NTS}: fraction of product with only the nontarget-strand (NTS) nicked; $L_{TS,NTS}$: fraction of linear product generated from the TS-pathway (i.e., first cut on TS by HNH and then the second cut on NTS by RuvC); $L_{NTS,TS}$: fraction of linear product

generated from the NTS-pathway (i.e., first cut on NTS by RuvC and then the second cut on TS by HNH); *L*: fraction of total linear product; α, active fraction of the precursor; $k_{1,HNH}$, rate constant for nicking the TS of the precursor by the HNH domain; $k_{1,RuvC}$, rate constant for nicking the NTS of the precursor by the RuvC domain; $k_{2,HNH}$, rate constant for the HNH cleaving the TS of the nicked product produced by the RuvC domain; $k_{2,RuvC}$, rate constant for the RuvC cleaving the NTS of the nicked product produced by the HNH domain. The observed DNA cleavage rate constants are represented in units of min^{-1}.

Off-target analysis. The results of the off-target DNA cleavage assays were graphed using the average DNA linearization for three independent replications. Linear fraction was obtained by dividing the intensity of the linear band (L) by the sum of the intensities of the nicked (N), L, and supercoiled (SC) bands as follows:

$$\text{Frac (L)} = \frac{\text{L}}{\text{N}+\text{L}+\text{SC}} \quad (5)$$

In all DNA cleavage assays, standard error of the mean (SEM) of the DNA band intensity values was calculated to describe the variation among the replications.[31]

Set up of SpyCas9-NTS-DNA complex models for MD simulations

Initial structure of SpyCas9-NTS-DNA complex. Following literature precedence,[34] models for MD simulation were obtained by stripping sgRNA and TS-DNA from the structural ensemble of a catalytically active SpyCas9 complex that was developed for our previous study (full active state of model B[18] that contains SpyCas9-sgRNA-TS-DNA-NTS-DNA derived from the experimental structure PDB ID: 5F9R).[12] SpyCas9^{WT}-NTS-DNA-Mn^{2+} came from SpyCas9^{WT}-NTS-DNA-Mg^{2+} *via* Mn^{2+} replacement. SpyCas9^{H982A}-NTS-DNA-Mn^{2+} was set up by substituting His982 to Ala in SpyCas9^{WT}-NTS-DNA-Mn^{2+}. The results of Figure 5 and Supplementary Figures S1B, S10, S11, and S13 in the Supplementary Information were based on these models.

Set up of SpyCas9-NTS-DNA ion-perturbation model. Based on the two-metal-ion model for SpyCas9's RuvC cleavage, there are two catalytic Mg^{2+}/Mn^{2+} ions (Supplementary Fig. S1 in the Supplementary Information). The one closer to H982 is $Mg^{2+}{}_A/Mn^{2+}{}_A$, and the other one is $Mg^{2+}{}_B/Mn^{2+}{}_B$ (Fig. 6A).[35] Ion perturbation models were used to investigate the role of residue 982 in the recruitment of $Mg^{2+}{}_A/Mn^{2+}{}_A$ to the catalytic center. The original $Mg^{2+}{}_A/Mn^{2+}{}_A$ was removed and ten Mg^{2+}/Mn^{2+} ions were randomly placed around the RuvC enzymatic center. After equilibration, the new ion with the shortest distance to the originally removed $Mg^{2+}{}_A/Mn^{2+}{}_A$ location was named as ''perturbed $Mg^{2+}{}_A/Mn^{2+}{}_A$'' for analysis in Figure 6 (the bottom scheme for Fig. 6A). The results of Figures 6 and 7 and Supplementary Figures S12 and S14 in the Supplementary Information were based on these models.

Further details about procedures used for MD simulations, free energy of binding estimations (MM/GBSA and MM/PBSA), and other data analyses are in the Supplementary Information. No IRB approvals were required for this work.

Results

Residues in the RuvC active site of SpyCas9 contributes differently toward gRNA-free DNA cleavage

Previously we had shown that gRNA-free DNA cleavage is performed by the RuvC active site in SpyCas9.[25] We analyzed the configuration of amino acids, divalent metals, and nucleic acids in SpyCas9's RuvC endonuclease domain to select residues that may contribute uniquely to gRNA-free DNA cleavage. Analysis of the RuvC active site in apoCas9 (PDB ID: 4CMQ[10]) shows that essential residues for gRNA-dependent DNA cleavage (D10, E762, H983, and D986) and a nonessential residue E766 is involved in the octahedral coordination of the Mn^{2+} ions (Supplementary Fig. S1A in the Supplementary Information). Analyzing the RuvC active site in the MD traces for gRNA-free DNA cleavage, H982 is identified as the second shell coordinating residue for Mn^{2+}, with it being closer to $Mn^{2+}{}_A$ (Supplementary Fig. S1B in the Supplementary Information).

We selected E766 and H982 as possible candidates that can promote gRNA-free DNA cleavage without impacting gRNA-dependent DNA cleavage, possibly by structuring the catalytically competent state for gRNA-free DNA cleavage. We created combinations of E766A, H982A, and H983A variants (SpyCas9^{E766A}, SpyCas9^{H982A}, SpyCas9$^{E766/H982A}$, and SpyCas9$^{E766/H983A}$) to test the roles of these residues in gRNA-free DNA cleavage (Supplementary Fig. S2 in the Supplementary Information).

In vitro gRNA-free DNA cleavage showed that SpyCas9^{E766A} does not remove gRNA-free cleavage activity (Supplementary Fig. S2A in the Supplementary Information). SpyCas9^{H982A} has negligible gRNA-free DNA cleavage activity even at 500 nM protein concentration with Mn^{2+} (Supplementary Figs. S2B and S3 in the Supplementary Information); however, it is active for gRNA-dependent DNA cleavage with 100 nM Cas9-sgRNA

(RNP) concentration (Supplementary Fig. S2E in the Supplementary Information). The double substitution variant SpyCas9$^{E766A/H982A}$ does not noticeably decrease the gRNA-free activity relative to the single substitution variant SpyCas9^{H982A} (Supplementary Fig. S2B and C in the Supplementary Information), so the SpyCas9^{H982A} variant was chosen for further in-depth analyses toward its role in gRNA-free DNA cleavage.

His982 of SpyCas9's RuvC active site is a major enhancer of gRNA-free DNA cleavage

To analyze the effect of H982 on gRNA-free DNA cleavage, we tested gRNA-free DNA cleavage with different divalent metal ions at two different concentrations (Fig. 1A and Supplementary Fig. S4 in the Supplementary Information). Results from a two-sided *t*-test showed that the H982A substitution significantly impairs the ability of SpyCas9 to catalyze gRNA-free DNA cleavage with 1 and 10 mM Mn^{2+}, 1 mM Co^{2+}, and 10 mM Ni^{2+}. In SpyCas9^{H982A}, gRNA-free DNA cleavage is reduced by 74% and 96% for 1 and 10 mM Mn^{2+}, respectively, 53% for 1 mM Co^{2+}, and 100% for 10 mM Ni^{2+} (Fig. 1B).

Divalent metal titration assays with Mn^{2+} and Co^{2+} showed that gRNA-free DNA cleavage is concentration-dependent and that the H982A substitution inhibits gRNA-free DNA cleavage at higher metal concentrations compared to SpyCas9^{WT} (Supplementary Fig. S5 in the Supplementary Information). SpyCas9^{WT} can completely degrade all the substrate with 25 μM Mn^{2+} (10 μM also induces significant gRNA-free DNA cleavage with SpyCas9^{WT}), while a significant amount ($\sim$76%) of the substrate is left uncleaved at 10 mM Mn^{2+} in the case of SpyCas9^{H982A}. For Co^{2+}, SpyCas9^{WT} completely degraded all the substrate at a concentration of 100 μM, while SpyCas9^{H982A} required 500 μM Co^{2+} to achieve this (Supplementary Fig. S5 in the Supplementary Information). The results indicate that based on the sidechain substitution and the type of divalent metal, SpyCas9 RuvC varies in its ability to catalyze gRNA-free DNA cleavage.

To quantify the inhibition of gRNA-free DNA cleavage by the H982A substitution, we measured the rate constants (k_{obs}) for the disappearance of the single-stranded M13mp18 DNA substrate at different conditions (Fig. 2, Supplementary Fig. S6 in the Supplementary Information, and Table 1).

Compared to SpyCas9^{WT}, the H982A substitution reduced the gRNA-free DNA cleavage rate constant by $\sim$167-fold with Mn^{2+} and $\sim$18-fold with Co^{2+} (Fig. 2, Supplementary Fig. S6 in the Supplementary Information, and Table 1). While both Mn^{2+} and Co^{2+} can promote gRNA-free DNA cleavage at a similar efficiency in SpyCas9^{WT} ($\sim$1 and 0.7 min^{-1} respectively), there is an approximately sevenfold ($\sim$0.006 min^{-1} vs. $\sim$0.04 min^{-1}) difference between the k_{obs} of SpyCas9^{H982A} obtained with Mn^{2+} and Co^{2+} (Table 1). These observations strongly support our idea that RuvC residues and their interactions with divalent metal ions play a significant role in catalyzing gRNA-free DNA cleavage and that the effect is distinct based on the type of the divalent metal.

SpyCas9^{H982A} variant retains efficient gRNA-dependent DNA cleavage

Since gRNA-dependent DNA cleavage is essential for gene-editing applications, we proceeded to test the effect of H982A substitution in gRNA-dependent DNA cleavage (Fig. 3). Time-course experiments were carried using supercoiled DNA substrates with pre-formed Cas9-sgRNA complexes, and the data were analyzed with a parallel-sequential model, where SpyCas9 uses two independent pathways in a parallel fashion to linearize dsDNA.[18] One of the pathways is designated as the TS pathway, in which the DNA is first nicked at the TS by HNH with a rate constant of $k_{1,HNH}$, followed by linearization by RuvC with a rate constant of $k_{2,RuvC}$. In the parallel NTS pathway, the DNA is first nicked at the NTS by RuvC with a rate constant of $k_{1,RuvC}$, followed by linearization by HNH with a rate constant of $k_{2,HNH}$.[18]

The analyses yielded highly similar $k_{1,HNH}$ and $k_{1,RuvC}$ values for SpyCas9^{WT} and SpyCas9^{H982A} (Table 2). The ratio of ($k_{1,HNH}$+$k_{1,RuvC}$), which collectively reflects the decay of the supercoiled precursor to the nicked intermediates, was 1.01 between SpyCas9^{H982A} and SpyCas9^{WT} (Table 3), indicating that the H982A substitution does not impact the first-step of nicking of the DNA. For the second-step of nicked to linear conversion, $k_{2,RuvC}$ and $k_{2,HNH}$ values showed differences between SpyCas9^{WT} and SpyCas9^{H982A} (Table 2). The ratio of ($k_{2,RuvC}$/$k_{1,HNH}$), which measures the efficiency of converting the TS nicked intermediate to linear product, was 0.007 between SpyCas9^{H982A} and SpyCas9^{WT} (Table 3), indicating that the H982A substitution impairs nicked to linear conversion through the TS-pathway by $\sim$100-fold.

On the other hand, the ratio of ($k_{2,HNH}$/$k_{1,RuvC}$), which measures the efficiency of converting the NTS nicked intermediate to linear product, was $\sim$17 between SpyCas9^{H982A} and SpyCas9^{WT} (Table 3), indicating that the H982A substitution enhances linearization through the NTS-pathway by $\sim$17-fold. With differential impacts on the TS- and NTS-pathways, SpyCas9^{H982A} is slower in the overall conversion of nicked to linear DNA (Fig. 3A, B). Additionally, gRNA-dependent DNA cleavage without preincubation of Cas9 and sgRNA before

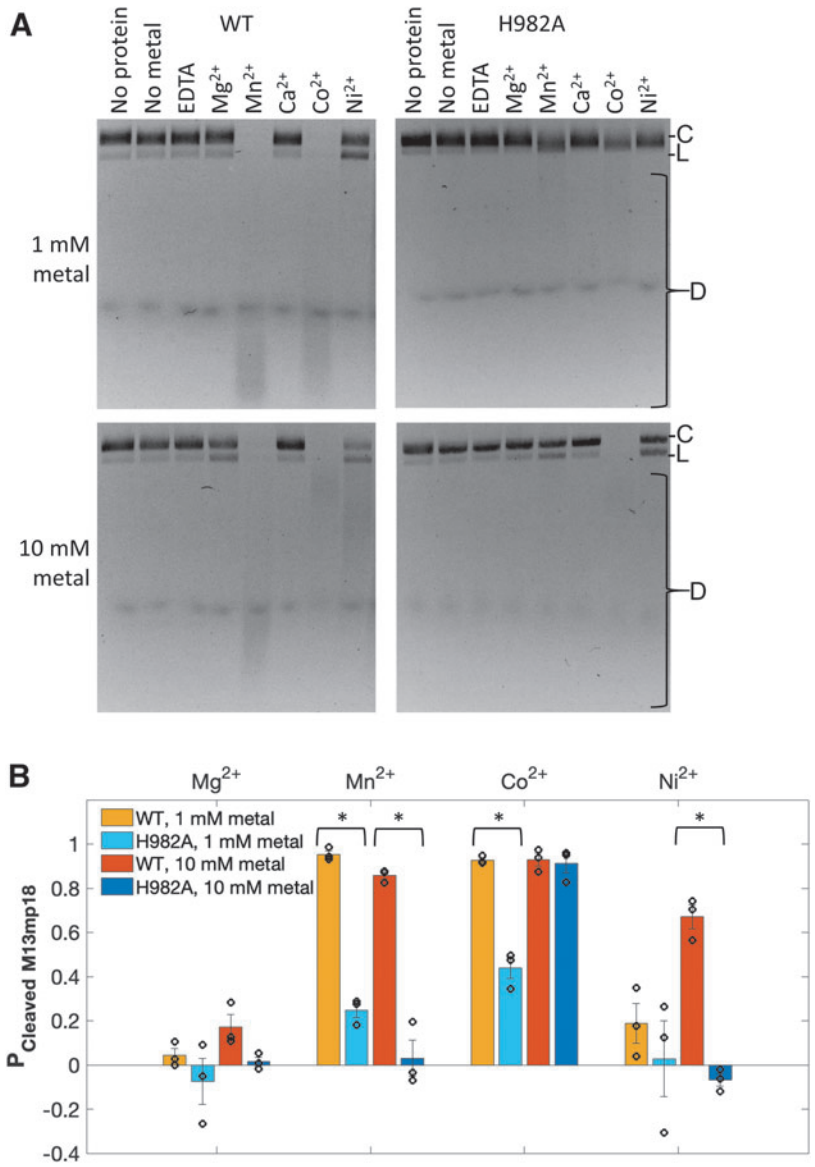

FIG. 1. Divalent metal dependence of gRNA-free DNA cleavage. **(A)** Representative agarose gels that were quantified to construct the bar graph in **(B)** (total reaction time = 30 min). Supplementary Figure S4 in the Supplementary Information has the uncropped gels and shows a wider variety of metals. **(B)** The fraction of cleaved single-stranded M13mp18 DNA [$P_{\text{cleaved M13mp18}} = 1\text{-}P_{\text{M13mp18}}$, with P_{M13mp18} defined by Eq. (1a), $P_{\text{cleaved M13mp18}}$] is plotted for four conditions: SpyCas9^{WT} (WT) and SpyCas9^{H982A} (H982A) protein, and 1 and 10 mM divalent metal. As observed, Mg^{2+} was expected to have very little gRNA-free DNA cleavage with SpyCas9^{WT}. Also as observed, Mn^{2+}, Co^{2+}, and Ni^{2+} were expected to facilitate significant gRNA-free DNA cleavage in SpyCas9^{WT}. The error bars plotted are SEM of three replications shown as black circles. According to the two-sample *t*-test, there is a significant difference between the SpyCas9^{WT} and SpyCas9^{H982A} for 1 and 10 mM Mn^{2+}, 1 mM Co^{2+}, and 10 mM Ni^{2+}. *$p \leq 0.001$. C, circular; D, degraded; L, linear; SEM, standard error of the mean; SpyCas9^{WT}, wild-type SpyCas9; WT, wild-type; SpyCas9^{H982A}, H982A-variant of SpyCas9; H982A, H982A variant.

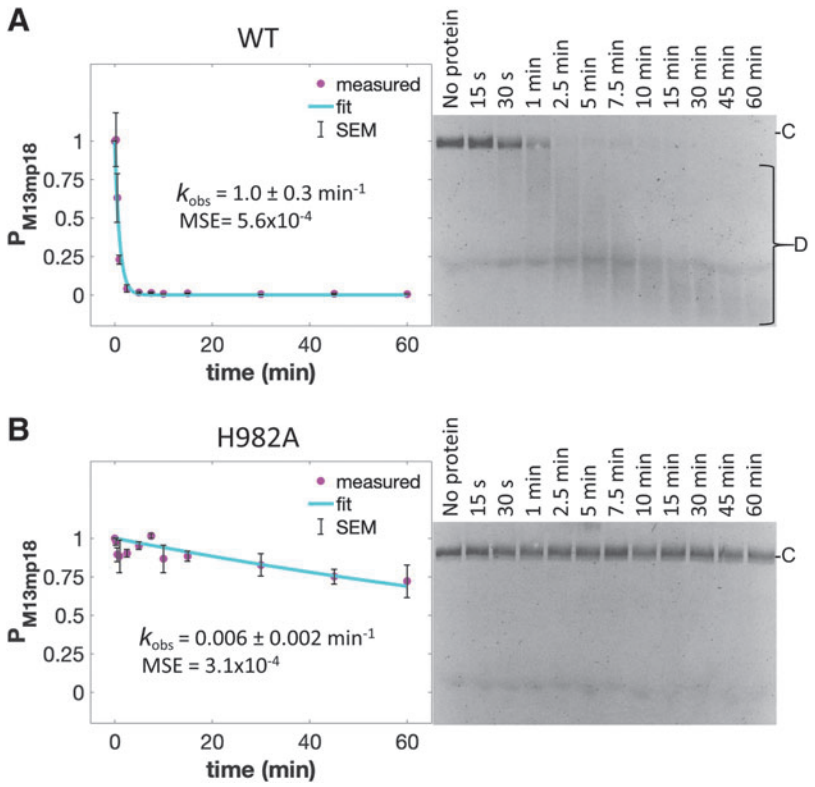

FIG. 2. Rate constants (k_{obs}, min^{-1}) and representative gels for gRNA-free cleavage of single-stranded M13mp18 DNA with Mn^{2+}. Single exponential fit [cyan line, Eq. (1b)] of average fraction of uncleaved DNA [Eq. (1a), $P_{M13mp18}$] plotted against time (t, min) for **(A)** SpyCas9^{WT}-Mn^{2+} and **(B)** SpyCas9^{H982A}-Mn^{2+}. The data points (magenta) are the average of three replications with SEM shown as error bars. MSE represents the deviation of data points from the single exponential fit line. The error reported for k_{obs} is the 95% confidence interval determined with the MATLAB fitting program. C, circular; D, degraded; MSE, mean square error; SEM, standard error of the mean.

adding the DNA precursor yielded slower, yet comparable results (Supplementary Fig. S7 in the Supplementary Information). There is a 5-fold increase in DNA linearization through the NTS-pathway in this experiment (Supplementary Fig. S7 in the Supplementary Information). Taken together, with a similar level of nicking and the modified use of NTS-pathway, we conclude this variant to possess acceptable levels of gRNA-dependent DNA cleavage while maintaining >150-fold reduction in gRNA-free DNA cleavage.

Table 1. Rate constants for guide RNA-free DNA cleavage measured from the single exponential fitting [k_{obs}, Eq. (1b)] of data shown in Figure 2 and Supplementary Figure S6 in the Supplementary Information

Enzyme-divalent metal	k_{obs} *(min^{-1})*
SpyCas9^{WT}-Mn^{2+}	1.0 ± 0.3
SpyCas9^{H982A}-Mn^{2+}	0.006 ± 0.002
SpyCas9^{WT}-Co^{2+}	0.7 ± 0.4
SpyCas9^{H982A}-Co^{2+}	0.04 ± 0.01

SpyCas9^{WT}, wild-type SpyCas9; SpyCas9^{H982A}, H982A-variant of SpyCas9.

To assess the impact of H982A substitution in Cas9's DNA cleavage using the two independent endonuclease domains, we performed FAM-labeled oligo DNA cleavage assays to monitor individual DNA cleavages by the HNH domain and the RuvC domain (Supplementary Figs. S8 and S9 in the Supplementary Information). The results show that cleavage by the HNH domain of both SpyCas9^{WT} and SpyCas9^{H982A} are similar (Supplementary Fig. S8 in the Supplementary Information), while differences are observed in the RuvC cleavage (Supplementary Fig. S9A in the Supplementary Information).

To quantify the effect on RuvC cleavage, we calculated rate constants for NTS cleavage by SpyCas9^{H982A} (Supplementary Fig. S9B in the Supplementary Information) and SpyCas9^{WT} (Supplementary Fig. S9C in the Supplementary Information). For SpyCas9^{WT}, we were able to adequately fit NTS cleavage to a single-exponential decay with a large k_{obs} ($\sim 5\,min^{-1}$). For

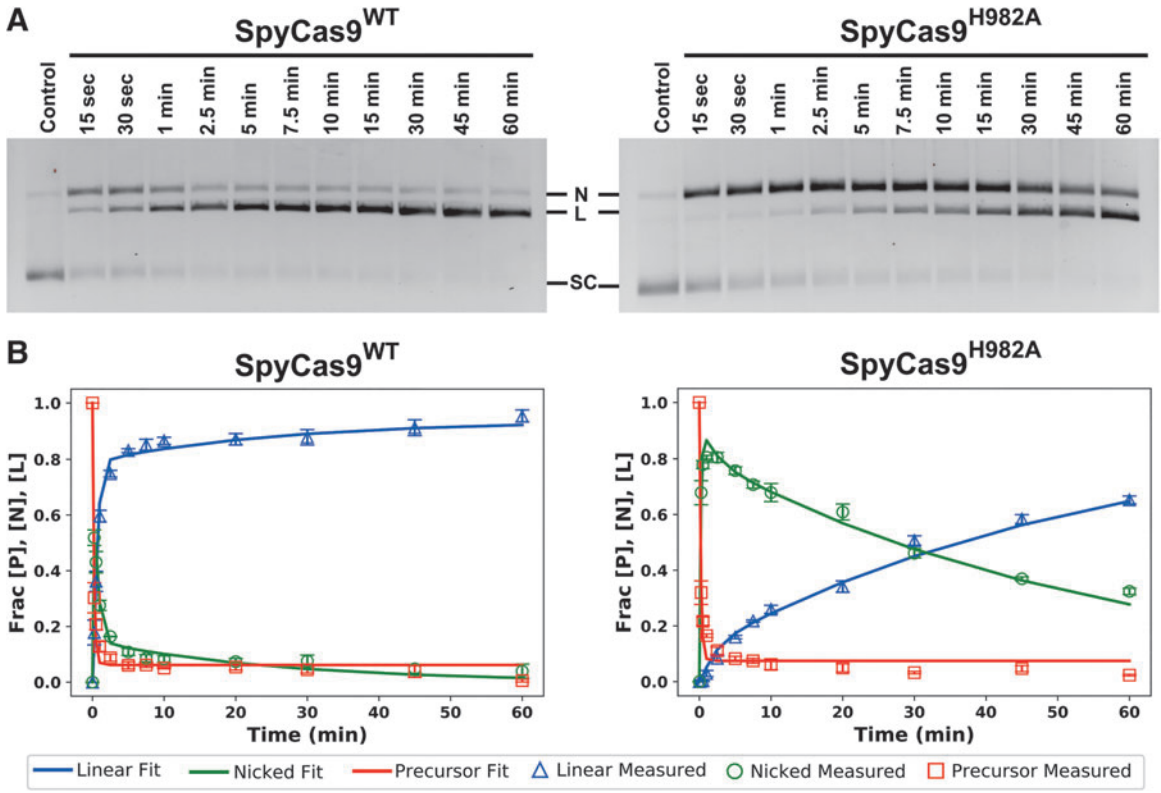

FIG. 3. Assessment of gRNA-dependent DNA cleavage at 37°C with Mg^{2+}. Reactions were performed after preincubation of Cas9-gRNA to form the binary complex before the addition of supercoiled substrate DNA. **(A)** Representative gels for gRNA-dependent DNA cleavage with preincubation of Cas9 and sgRNA. **(B)** Graphs showing the global fit of the precursor (P), nicked (N), and linear (L) forms of DNA in the gRNA-dependent DNA cleavage reactions catalyzed by $SpyCas9^{WT}$ and $SpyCas9^{H982A}$. We used a parallel sequential model that we described previously[18] for data analysis [Eqs. (2–4)]. Results from a similar experiment where Cas9 and sgRNA were not preincubated is shown in Supplementary Figure S7 in the Supplementary Information. sgRNA, single guide RNA.

$SpyCas9^{H982A}$, we were able to adequately fit NTS cleavage only to a double-exponential decay. The k_{fast} is large ($\sim 4\,min^{-1}$), which is similar to k_{obs} for RuvC cleavage by $SpyCas9^{WT}$. These data show that H982A substitution alters the cleave mechanism of RuvC slightly without negatively impacting HNH cleavage and that the effect on gRNA-dependent DNA cleavage does not significantly reduce DNA linearization by the variant.

His982Ala substitution selectively enhances DNA mismatch sensitivity of SpyCas9

We tested whether the H982A substitution decreases DNA cleavage when there is an imperfect complementarity between the guide region of the gRNA and the DNA substrate, which will assess its off-target DNA cleavage sensitivity. A selected set of DNA substrates with a single mismatch at the 3rd, 5th, or 18th nt (MM3, MM5, and

Table 2. Kinetic parameters obtained from fitting to the parallel-sequential model for gRNA-dependent DNA cleavage by $SpyCas9^{WT}$ and $SpyCas9^{H982A}$

Enzyme	*Active fraction*	$k_{1,HNH}$ (min^{-1})	$k_{2,RuvC}$ (min^{-1})	$k_{1,RuvC}$ (min^{-1})	$k_{2,HNH}$ (min^{-1})
$SpyCas9^{WT}$	0.94 ± 0.02	4.00 ± 0.55	2.25 ± 0.36	0.74 ± 0.21	0.04 ± 0.02
$SpyCas9^{H982A}$	0.93 ± 0.02	4.20 ± 0.66	0.02 ± 0.00	0.59 ± 0.27	0.55 ± 0.67

The experiment was conducted at 37°C with preincubation of Cas9 and gRNA to form the binary complex. Controls showed that the fitted value reported here were independent of the starting trial values, indicating that the experimental data sets can be sufficiently analyzed by the parallel-sequential model. The uncertainty ranges, which were obtained from the fitting program, gave a larger value for $k_{2,HNH}$ of $SpyCas9^{H982A}$ as compared to the other parameters, the reason behind this is unclear.

gRNA, guide RNA.

Table 3. Comparison of the relative use of target-strand and nontarget-strand pathways

Enzyme	$k_{1,HNH}+k_{1,RuvC}$	$k_{2,RuvC}/k_{1,HNH}$	$k_{2,HNH}/k_{1,RuvC}$
SpyCas9^{WT}	4.74	0.563	0.054
SpyCas9^{H982A}	4.79	0.005	0.932
SpyCas9^{H982A}/ SpyCas9^{WT} ratio	1.01	0.01	17.26

MM18, respectively) position downstream of the PAM was used for gRNA-dependent off-target DNA cleavage assays. The total reaction time for this assay is 15 min using Mg^{2+} as the divalent metal ion. Previous studies have shown that PAM-proximal mismatches are cleaved at varying efficiencies by SpyCas9 based on the mismatch position, whereas as PAM-distal mismatches are cleaved at similar efficiencies as the completely matched DNA.[7,36] The results from our mismatch cleavage assay showed that SpyCas9^{H982A} generally has a lower efficiency in linearizing DNA substrates with a corresponding accumulation of nicked DNA (Fig. 4A).

Comparing the different mismatches, SpyCas9^{H982A} was better than SpyCas9^{WT} at discriminating a mismatch at position 5 (Fig. 4B). To further assess the specificity effects, we calculated MCH/MM for each protein to find the discrimination effect compared to the efficiency of cleaving matched (MCH) DNA (Fig. 4C). The results show that SpyCas9^{H982A} is more selective relative to SpyCas9^{WT} for MM5 since the ratio of matched DNA cleaved to that of MM5 is higher for SpyCas9^{H982A} than for SpyCas9^{WT}. For MM18, even though SpyCas9^{H982A} has lower total linear DNA compared to SpyCas9^{WT} (Fig. 4B), the MCH/MM18 ratio shows that both proteins have the same level of selectivity against mismatches in the 18th nt position. For MM3, SpyCas9^{WT} shows more discrimination than SpyCas9^{H982A} (Fig. 4C). These results show that SpyCas9^{H982A} has a slightly improved mismatch discrimination toward the PAM-proximal DNA mismatches, which is dependent on the position of the mismatch with respect to the PAM.

Relative to Mg^{2+}, Mn^{2+} enhances NTS-DNA: SpyCas9^{WT}:divalent metal ion interactions in a gRNA-free environment, but the H982A substitution prevents this enhancement.

To elucidate the effects of the H982A substitution in gRNA-free DNA cleavage, we performed three sets of 500 ns MD simulations after removing gRNA and TS-DNA from the MD structure (SpyCas9^{WT}-gRNA-TS-DNA-NTS-DNA-Mg^{2+}) from our previous study[18]: (1) SpyCas9^{WT} complexed with NTS-DNA and Mg^{2+} (SpyCas9^{WT}-NTS-DNA-Mg^{2+}), (2) SpyCas9^{WT} complexed with NTS-DNA and Mn^{2+} (SpyCas9^{WT}-NTS-DNA-Mn^{2+}), and (3) SpyCas9^{H982A} complexed with NTS-DNA and Mn^{2+} (SpyCas9^{H982A}-NTS-DNA-Mn^{2+}) (Fig. 5A, B).

Our results showed significant differences for the three settings at the SpyCas9-NTS-DNA interface. Measuring the interactions within 2.5 Å between SpyCas9 and the entire length of the NTS-DNA, SpyCas9^{WT}-NTS-DNA-Mn^{2+} showed more contacts (average number = 131) than SpyCas9^{WT}-NTS-DNA-Mg^{2+} (average number = 116) and SpyCas9^{H982A}-NTS-DNA-Mn^{2+} (average number = 115) (Fig. 5C). These results indicate that in the absence of gRNA, Mn^{2+} facilitates more contacts between SpyCas9 and NTS-DNA than does Mg^{2+}; however, the H982A substitution prevents Mn^{2+} from facilitating those contacts. The free energy calculations further support the result of the contact analyses. SpyCas9^{WT}-NTS-DNA-Mn^{2+} showed lower free energy of binding between SpyCas9^{WT} and NTS-DNA (-200.1 ± 19.82 kcal/mol) than SpyCas9^{WT}-NTS-DNA-Mg^{2+} (-175.7 ± 17.07 kcal/mol) and SpyCas9^{H982A}-NTS-DNA-Mn^{2+} (-181.8 ± 12.42 kcal/mol) (Fig. 5D).

The contact analysis between NTS-DNA and SpyCas9 suggests that Mn^{2+} enhances the interactions between the NTS-DNA and SpyCas9 at multiple locations. Several key residues of SpyCas9 contributed to the interactions in SpyCas9^{WT}-NTS-DNA-Mn^{2+}, but such interactions are absent in SpyCas9^{WT}-NTS-DNA-Mg^{2+} and SpyCas9^{H982A}-NTS-DNA-Mn^{2+} in our simulations. The distances of DG-7P@H22–Lys 961@HG2, DC-3P@H3′–Asn 14@OD1, and DC-3P@H5′–Thr 13@OG1 were maintained within 2.5 Å in SpyCas9^{WT}-NTS-DNA-Mn^{2+} (Supplementary Fig. S10A and B in the Supplementary Information; purple lines in Supplementary Fig. S10C–E in the Supplementary Information), but these interactions were partially lost in SpyCas9^{WT}-NTS-DNA-Mg^{2+} (green lines in Supplementary Fig. S10C–E in the Supplementary Information) and SpyCas9^{H982A}-NTS-DNA-Mn^{2+} (red lines in Supplementary Fig. S10C–E in the Supplementary Information). The comparisons imply that Mn^{2+} improves overall interactions between SpyCas9^{WT} and NTS-DNA, but the H982A substitution reverses the effects of Mn^{2+}.

To assess the stabilization of the RuvC catalytic center, we compared key interactions between NTS-DNA and catalytic ions (Mg^{2+}/Mn^{2+}) that were placed in the catalytic center based on the positions of $Mn^{2+}{}_A$ and $Mn^{2+}{}_B$ in an experimental structure (PDB ID: 4CMQ),[10] where both the metals are present at a distance competent for DNA cleavage. In our simulations representing a gRNA-free condition, $Mn^{2+}{}_A$, but not $Mg^{2+}{}_A$, formed a new interaction with DC-3P (@OP2); however, the H982A substitution disrupted this interaction (Supplementary

Fig. S11 in the Supplementary Information), thus indicating H982's role in maintaining DNA close to the catalytic center.

H982A substitution impairs Mn^{2+} recruitment in the RuvC catalytic center

To test if H982 assists Mn^{2+} recruitment and stabilization of the RuvC catalytic center, we perturbed the RuvC catalytic center by removing the $Mg^{2+}{}_A/Mn^{2+}{}_A$, which coordinates with Asp10 and Asp 986 (the upper scheme in Fig. 6A), and randomly added 10 new Mg^{2+}/Mn^{2+} ions close to the RuvC catalytic center at the beginning of our MD simulations (the bottom scheme in Fig. 6A). We measured the distance between Asp 10 and $Mg^{2+}{}_A/Mn^{2+}{}_A$ during the simulation window of 100–500 ns (Fig. 6C) and showed the distance distribution between D10 and $Mg^{2+}{}_A/Mn^{2+}{}_A$ in Figure 6B.

The interaction between D10 and the metal (A) in SpyCas9^{WT}-NTS-DNA-Mg^{2+} is at 4.4 Å (green line in Fig. 6B; Supplementary Fig. S12A in the Supplementary Information), while it decreases to ~2 Å in SpyCas9^{WT}-NTS-DNA-Mn^{2+} (purple line in Fig. 6B), suggesting the stabilized coordination between the oxygen of Asp 10 and $Mn^{2+}{}_A$ ready for DNA cleavage (Supplementary Fig. S12B in the Supplementary Information).

In SpyCas9^{H982A}-NTS-DNA-Mn^{2+} simulations, the $Mn^{2+}{}_A$ moves very far from the RuvC catalytic center (~54 Å; red line in Fig. 6B; Supplementary Fig. S12C in the Supplementary Information). We also noticed that there is a disassociation between Asp 10 and $Mg^{2+}{}_A$, with $Mg^{2+}{}_A$ interacting with the negatively charged atom nearby (DC-3P@OP2) (Supplementary Fig. S12A in the Supplementary Information). In comparison, the ensemble from SpyCas9^{WT}-NTS-DNA-Mn^{2+} (Supplementary Fig. S12B in the Supplementary Information) showed that two Mn^{2+} ions are well-coordinated with D10 due to the formation of a new coordination between -4P and $Mn^{2+}{}_A$, providing the ideal two-metal-ion catalytic distances,[35] which will favor gRNA-free DNA cleavage with Mn^{2+}, and not with Mg^{2+}.

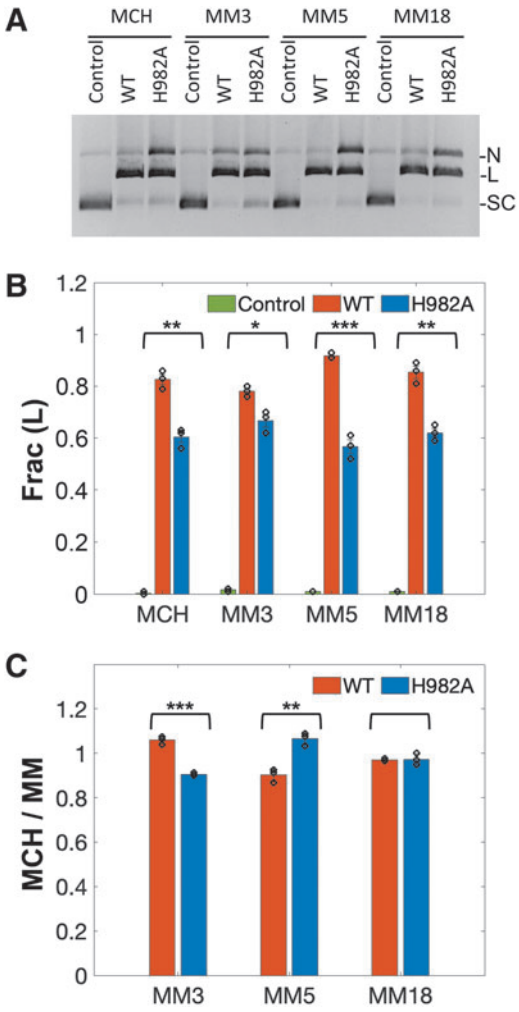

FIG. 4. Mismatched DNA substrate cleavage assay to assess on-target selectivity (off-target discrimination). The activity being tested is SpyCas9's gRNA-dependent DNA cleavage of supercoiled, double-stranded pUC19 DNA in the presence of Mg^{2+}, and the DNA substrates vary based on the presence of mismatches between the gRNA and the TS-DNA at positions 3 (MM3), 5 (MM5), and 18 (MM18) nucleotides away from the PAM. Total reaction time is 15 min. **(A)** Representative gel and **(B)** quantification of fraction of DNA linearized for each lane [Eq. (5)]. Control reactions have no protein. According to the two-sample *t*-test with a *p*-value of 0.05, there is a significant difference between SpyCas9^{WT} (WT) and SpyCas9^{H982A} (H982A) for each substrate type. **(C)** Graph of the ratio of the fraction of matched DNA linearized over the fraction of mismatched DNA linearized (MCH/MM) such that a high ratio corresponds to greater selectivity for cleavage of the MCH substrate relative to the mismatch substrate. According to the two-sample *t*-test with a *p*-value of 0.05, there is a significant difference between the WT and H982A MCH/MM with MM3 (where SpyCas9^{WT} is more specific than SpyCas9^{H982A}) and with MM5 (where SpyCas9^{H982A} is more specific than SpyCas9^{WT}), but not with MM18. The error bars plotted are SEM of three replications shown as black circles. $^*p \le 0.05$, $^{**}p \le 0.01$, $^{***}p \le 0.001$. MM, mismatches; PAM, protospacer adjacent motif; SpyCas9, *Streptococcus pyogenes* Cas9; TS-DNA, target strand DNA.

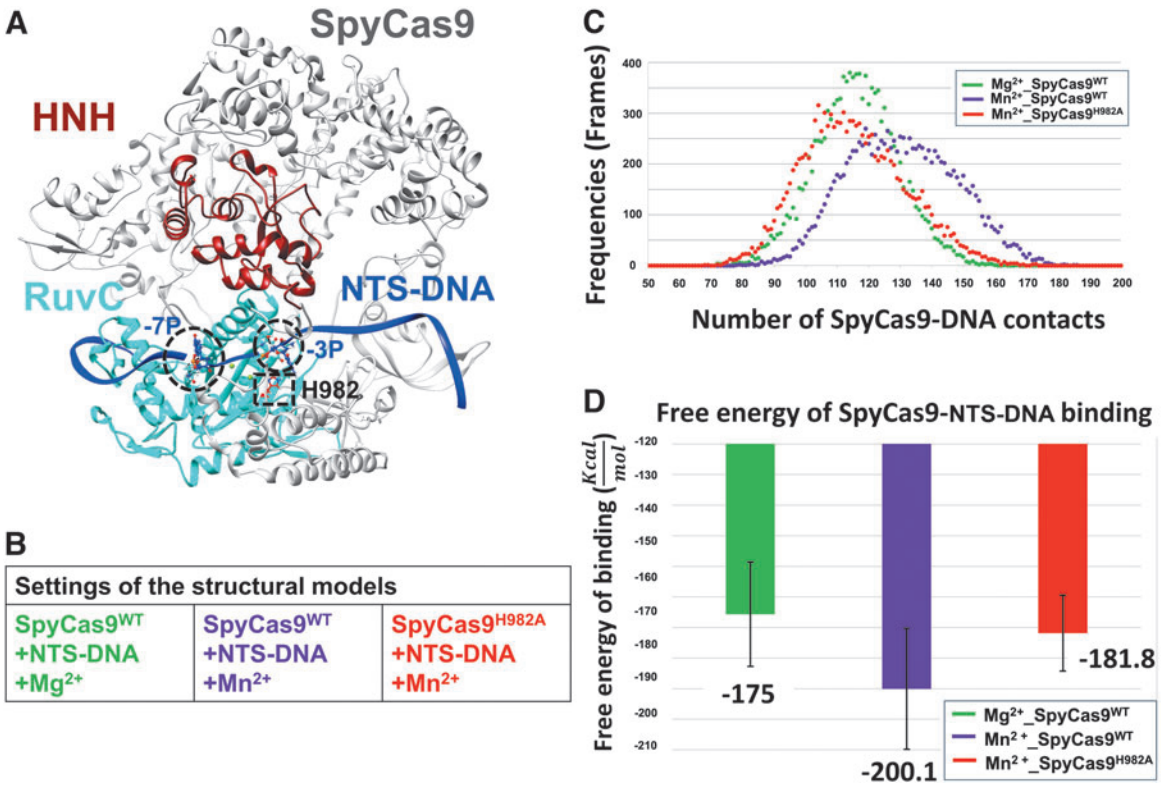

FIG. 5. Comparison of the interactions between SpyCas9^{WT}/SpyCas9^{H982A} and NTS-DNA. **(A)** Structural model of SpyCas9 complexed with NTS-DNA for MD simulation. HNH and RuvC are the two endonuclease domains of SpyCas9. The model is based on the SpyCas9 complex developed for our previous study (full active state of model B[18] after stripping sgRNA and TS-DNA). The dashed black rectangle denotes the location of residue H982 in SpyCas9. The dashed black circles highlight the interactions between NTS-DNA and SpyCas9. **(B)** Three structural settings for comparisons in this study. **(C)** The distributions of the average number of contacts between SpyCas9^{WT}/SpyCas9^{H982A} and NTS-DNA during simulations (note that atom distances between Cas9 and NTS-DNA within 2.5 Å are considered as contacts). (100–400 ns; accumulated 12,000 frames.) **(D)** Free energy of binding between SpyCas9^{WT}/SpyCas9^{H982A} and NTS-DNA in simulations *via* molecular mechanics generalized Born surface area calculation. (200–300 ns; accumulated 3000 frames.) MD, molecular dynamics; NTS-DNA, nontarget strand DNA.

We further calculated the free energy of binding (Δ) between $Mg^{2+}{}_A/Mn^{2+}{}_A$ and the rest of complex using molecular mechanics generalized Born surface area analysis which demonstrated that Δ of SpyCas9^{WT}-NTS-DNA-Mn^{2+} ($\Delta = -22.6 \pm 3.32$ kcal/mol) was lower than Δ of SpyCas9^{WT}-NTS-DNA-Mg^{2+} ($\Delta = 36.0 \pm 3.48$ kcal/mol) (Fig. 6D). The binding free energy analysis demonstrates that the ensemble of SpyCas9^{WT}-NTS-DNA-Mn^{2+} is the energetically favored structure for DNA cleavage. The negatively charged residues Asp10, Asp986, and -4P of NTS-DNA play a crucial role in generating a significantly negative binding free energy between $Mn^{2+}{}_A$ and SpyCas9^{WT}-NTS-DNA, as evidenced by Supplementary Tables S4 and S5 and Supplementary Figure S12 in the Supplementary Information. However, this contribution is lost when $Mn^{2+}{}_A$ is replaced with Mg^{2+}, resulting in a positive binding free energy for the SpyCas9^{WT}-NTS-DNA-Mg^{2+} system.

We note that the choice of water models can have an impact on the thermodynamic and kinetic properties of magnesium binding affinity, as suggested by previous studies.[37,38] Therefore, conducting additional comparisons using different water models would provide a better understanding of the observed differences in the free energy of binding analysis. Together, the ion perturbation analysis implies that H982 plays an important role in Mn^{2+} recruitment and stabilization in the absence of gRNA, supporting the deactivation of gRNA-free DNA cleavage in SpyCas9^{H982A}.

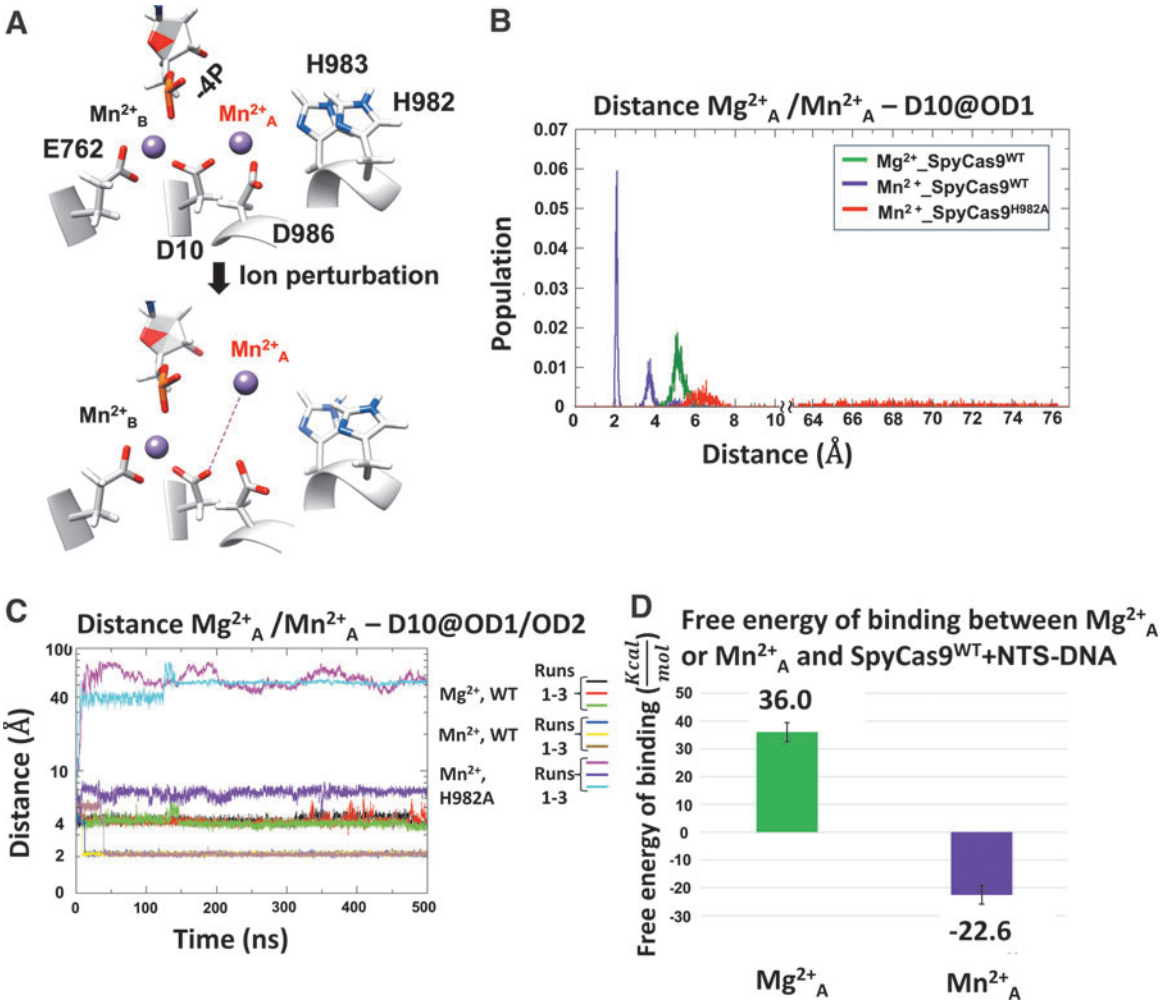

FIG. 6. Ion perturbation results comparing the ability of SpyCas9^{WT} versus SpyCas9^{H982A} RuvC to recruit Mg^{2+}/Mn^{2+}. **(A)** Scheme of ion perturbation using SpyCas9^{WT}-NTS-DNA-Mn^{2+} as an example. The upper scheme presents the well-coordinated $Mn^{2+}{}_A$ and $Mn^{2+}{}_B$, before $Mn^{2+}{}_A$ removal. The bottom scheme shows the newly added Mn^{2+} that is nearest the original location of $Mn^{2+}{}_A$. **(B)** Distance distribution of the interactions between D10 (@OD1) and perturbed $Mg^{2+}{}_A$/$Mn^{2+}{}_A$ in simulations. **(C)** Distance of the interactions between D10 (@OD1/OD2) and perturbed $Mg^{2+}{}_A$/$Mn^{2+}{}_A$ in 0–500 ns simulations. **(D)** Free energy of binding between $Mg^{2+}{}_A$/$Mn^{2+}{}_A$ and SpyCas9^{WT} complexed with nontarget strand DNA (NTS-DNA) in simulations *via* molecular mechanics generalized Born surface area calculation.

FIG. 7. The role of a water molecule in the Mn^{2+} recruitment. **(A, B)** The representative structure of SpyCas9^{WT}-NTS-DNA-Mn^{2+} before **(A)** and after **(B)** the formation of $Mn^{2+}{}_A$-D10 coordination. **(C)** The representative structure of SpyCas9^{H982A}-NTS-DNA-Mn^{2+}shown after $Mn^{2+}{}_A$ moves away from D10. **(D, E)** Distance analysis for the $Mn^{2+}{}_A$-D10 reconnection and the water dissociation in SpyCas9^{WT}-NTS-DNA-Mn^{2+}. **(D)** Distance analysis for $Mn^{2+}{}_A$–D10 @OD2 (H982). **(E)** Distance analysis for $Mn^{2+}{}_A$–WAT @O (H982). **(F)** Distance analysis for H982@ND1–WAT@H2 for the water between the added Mn^{2+} and D10 interacting with H982 in SpyCas9^{WT}-NTS-DNA-Mn^{2+}. **(G, H)** Distance analysis for the $Mn^{2+}{}_A$-D10 departure and the water behavior in SpyCas9^{H982A}-NTS-DNA-Mn^{2+}. **(G)** Distance analysis for $Mn^{2+}{}_A$–D10 @OD2 (H982A). **(H)** Distance analysis for $Mn^{2+}{}_A$–WAT @O (H982A). **(I)** Distance analysis for H982A@O–WAT @H1 (H982A). "Wat/WAT" denoted as a water molecule. The dashed pink line shows the transition time point from **(A)** to **(B)**.

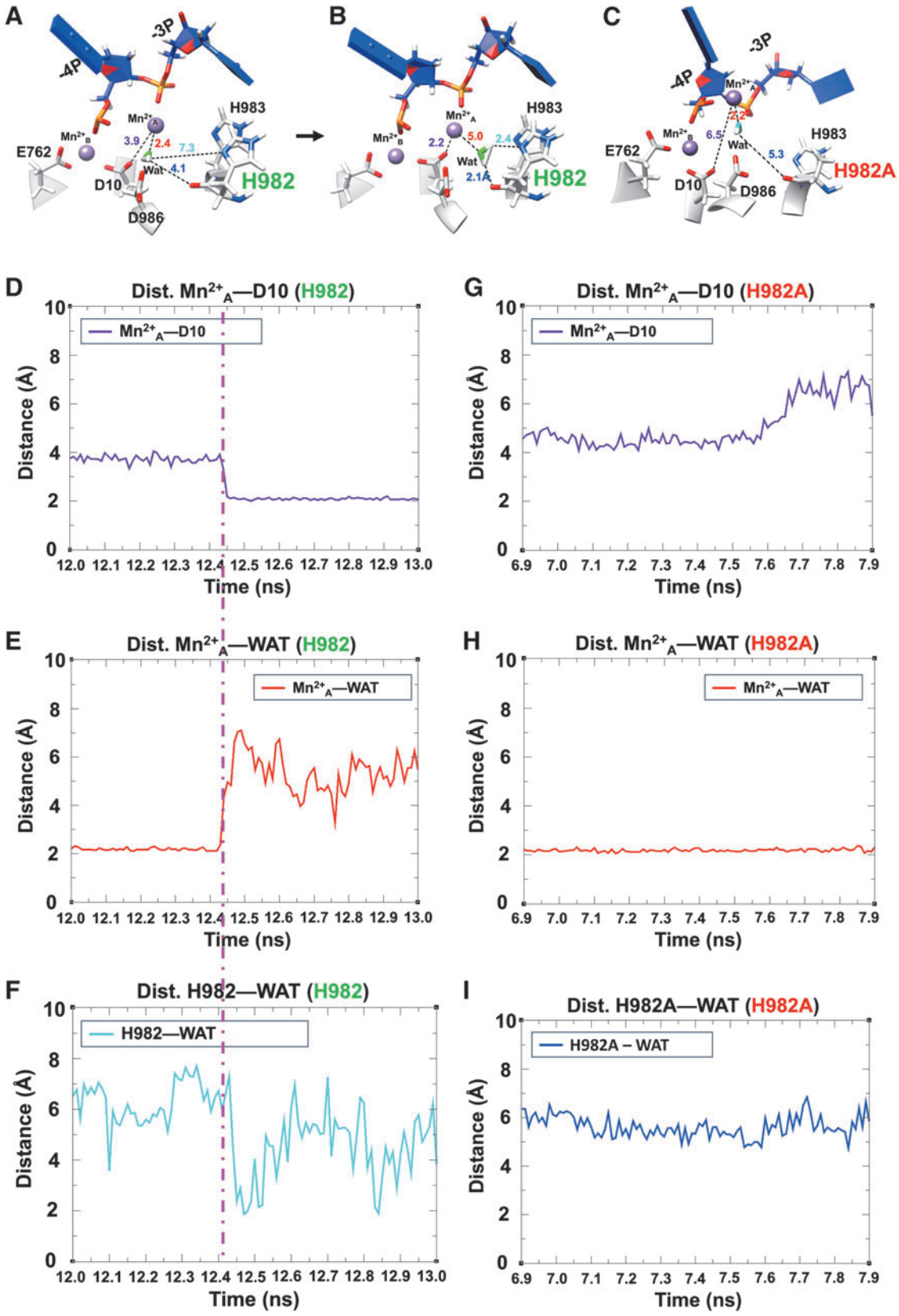

Proposed mechanism of gRNA-free DNA cleavage promoted by H982

To further investigate how H982 and H982A affect Mn^{2+} recruitment, we compared the trajectories of SpyCas9^{WT}-NTS-DNA-Mn^{2+} and SpyCas9^{H982A}-NTS-DNA-Mn^{2+} during the ion perturbation simulations. Initially in SpyCas9^{WT}-NTS-DNA-Mn^{2+}, a water molecule is observed coordinating with Mn^{2+}, preventing the recruitment of Mn^{2+} to orient D10 in for catalysis (Fig. 7A). Eventually, H982 pulls the water molecule away from $Mn^{2+}{}_A$ to facilitate the formation of a stable interaction between Mn^{2+} and D10 (Fig. 7B). When H982 was substituted with alanine, however, H982A was not able to pull water from $Mn^{2+}{}_A$ to expose $Mn^{2+}{}_A$ to form new coordination with D10 (Fig. 7C). Distance analysis was used to delineate the effect of the H982A substitution on the movements of WAT and $Mn^{2+}{}_A$ (Fig. 7D–F for H982 and Fig. 7G–I for H982A).

Based on these observations, we hypothesize that H982 might assist Mn^{2+} recruitment by pulling away the Mn^{2+}-coordinated water to facilitate the formation of an interaction between Mn^{2+} and D10. Since H982A cannot pull away the water molecule, it cannot facilitate the recruitment of Mn^{2+} to form the catalytic center. This hypothesis might explain why H982A reverses the effect of Mn^{2+} and impairs gRNA-free DNA cleavage activity.

Discussion

Differential regulation of the gRNA-free and RNA-guided DNA cleavage activities is possible because of different substrate and catalytic metal placement requirements

Our MD simulations suggest that Mn^{2+} promotes gRNA-free DNA cleavage by ideal placement of the single stranded-DNA (ssDNA) along the RuvC catalytic center such that it is accessible for DNA cleavage. Our MD simulations with the H982A substitution suggest that H982 is needed to recruit Mn^{2+} to the metal (A) position in RuvC, according to the two-metal-ion catalysis model, for Mn^{2+}-mediated ssDNA substrate positioning and cleavage. Since H982 is not required for the positioning of Mg^{2+} and dsDNA for RNA-guided DNA cleavage, the H982A substitution is a way to prevent gRNA-free ssDNA cleavage even in a gene-editing context, where Mn^{2+} is present in the cell. Further quantum mechanics/molecular mechanics calculations will help delineate the differences in the organization of the RuvC active site in the presence of gRNA with Mg^{2+} versus Mn^{2+} that are expected based on the difference in H982-dependence for metal recruitment and RNA-guided dsDNA cleavage rates.

A possible explanation for why Co^{2+} can still promote DNA cleavage is that the higher electronegativity of Co^{2+} may enable enhanced metal coordination even in the absence of H982. Nevertheless, an $\sim$18-fold reduction in the rate constant of SpyCas9^{H982A} compared to that in SpyCas9^{WT} indicates that H982 plays a role in stabilizing Co^{2+} under gRNA-free conditions.

RuvC active site of Cas9 is histidine-rich which provides flexibility in DNA cleavage mechanisms

There are three histidine residues (H982, H983, and H985) in SpyCas9's RuvC active site and their prevalence indicates that these residues may partially compensate for each other as general (Lewis) bases as indicated by the ability of imidazole to rescue the activity of the SpyCas9$^{H982A/H983D/H985A}$ variant.[30] Studies have shown that the main catalytic mediator for gRNA-dependent DNA cleavage is H983,[19] with a complete inactivity of ntDNA cleavage with a H983A substitution in the presence of Mg^{2+},[39] (Supplementary Fig. S2G in the Supplementary Information). Interestingly, Mn^{2+} can partially rescue the gRNA-dependent DNA cleavage activity in H983A or H983G substitutions, but its rescue effect is significantly reduced in H983G/H982A double substitution.[39] The extra histidine residues in the RuvC site may enable the enzyme to adapt to different types of DNA cleavage conditions and use Mn^{2+} as a catalytic metal for gRNA-free DNA cleavage activity.

Other enzymes such as eukaryotic topoisomerase II showed higher dsDNA cleavage activity in the presence of Mn^{2+}, Ca^{2+}, or Co^{2+} than in the presence of Mg^{2+}.[40] As ligands, Mg^{2+} and Mn^{2+} both prefer octahedral coordination geometry, but Mn^{2+} generally shows higher protein binding affinity than Mg^{2+} when the Irving–Williams series is applied to describe stability between divalent metals and metalloproteins.[41]

Our data shows that H982 plays a very prominent role in SpyCas9's gRNA-free DNA cleavage, with H982A substitution causing $\sim$167-fold reduction in Mn^{2+}-mediated gRNA-free DNA cleavage. MD simulation results showed that H982 directly contributes to Mn^{2+} recruitment, stabilizing $Mn^{2+}{}_A$-D10 interaction, and stabilizing Cas9-NTS-DNA interactions. Dürr et al. reported that in HIV-1 RNase H, the conserved histidine (H1126) not only serves as a general base for the enzymatic reaction but also serves as a recruiter of a third metal ion to facilitate product release in HIV-1 RNase H.[42] Our data implies that for SpyCas9's gRNA-free DNA cleavage, H983 still acts as the base, while H982 is involved in metal coordination and DNA binding, since a H982A variant is unable to perform gRNA-free DNA cleavage (Supplementary Fig. S2B in the Supplementary Information).

H982A substitution also contributes toward increased DNA mismatch discrimination. Our analysis using

selected DNA mismatches (Fig. 4) along with existing studies in the field shows that H982A substitution makes SpyCas9 more sensitive to DNA mismatches.[29,30] The H982A and H983D variants and the double variant (H982A/H983D) were able to discriminate mismatches in positions 1–19 with different efficiencies.[30] These results indicate that SpyCas9^{H982A} can reduce both gRNA-free and off-target DNA cleavages, two of the undesirable effects of SpyCas9-based genome applications.

RuvC is organized as an autonomous endonuclease that can access and cleave DNA without gRNA-dependent conformational changes

Previous studies have established that the conformational changes upon gRNA and DNA binding are essential for concerted cleavage needed to make a dsDNA break through gRNA-dependent DNA cleavage.[8–10,12,13] For gRNA-free DNA cleavage, these conformational changes seem to be dispensable for RuvC to cleave ssDNA. The fact that SpyCas9 preferentially degrades ssDNA by gRNA-free DNA cleavage points to RuvC's ability to accommodate only ssDNA in its catalytic center without the extensive conformational changes mediated by sgRNA binding.

It is possible that the improved SpyCas9-NTS-DNA interactions in the presence of Mn^{2+} that are mediated by H982 provides RuvC access and energetics to cleave DNA in a gRNA-free manner.[10] In this sense, gRNA-free DNA cleavage is much like the *trans*-DNA cleavage that is an aftermath of *cis*-cleavage in Cas12a, where the RuvC active site is exposed for progressive ssDNA degradation.[43,44] It can be envisioned that interactions of H982, Mn^{2+}, and ssDNA are similar to activation needed for Cas12a's *trans*-cleavage by keeping RuvC active site accessible for progressive degradation of ssDNA.

Conclusion

Divalent metals can fine-tune the activity of several nucleic-acid catalyzing enzymes. We utilized this property to engineer SpyCas9. Since SpyCas9 is a powerful tool for clinical gene therapy, it will raise critical concerns if its DNA cleavage specificity is impaired by certain divalent metal cations. Our current study offers perspectives on modulating divalent metal-binding properties to remove unwarranted DNA cleavages by Cas enzymes.

Accession Codes

SpyCas9 UniProt ID: Q99ZW2.

Acknowledgments

We thank the OU Protein Production & Purification Core (PPC Core) for protein purification services and instrument support. The OU PPC Core is supported by an IDeA grant from NIGMS (grant Nos. P20GM103640 and P30GM145423). We also acknowledge the use of computational resources provided by the High-Performance Computing (HPC) center at the University of North Texas (UNT).

Authors' Contributions

S.N.N., D.-S.W., H.P.P., J.L., and R.R. conceived the idea; S.N.N., D.-S.W., S.R., I.S., H.P.P., Y.G.J., J.L., and R.R. designed and performed experiments; S.N.N., D.-S.W., S.R., I.S., Y.G.J., P.Z.Q., J.L., and R.R. performed data analysis; S.N.N., D.-S.W., S.R., J.L., and R.R. wrote the manuscript; and all authors edited the manuscript. All authors have approved the current version of the manuscript.

Author Disclosure Statement

No conflicts of interest.

Funding Information

This work was supported in part by grants from the National Science Foundation (MCB-1716423, R.R.; MCB-1716744, P.Z.Q.), National Institution of General Medical Sciences (P.Z.Q., R35GM145341), Oklahoma Center for the Advancement of Science and Technology (OCAST) award (grant No. HR20-103, R.R.) and the J.L. members were supported by National Heart, Lung, and Blood Institute of the National Institutes of Health (R15HL147265).

Supplementary Material

Supplementary Data

References

1. Mojica FJ, Diez-Villasenor C, Garcia-Martinez J, et al. Intervening sequences of regularly spaced prokaryotic repeats derive from foreign genetic elements. J Mol Evol 2005;60(2):174–182; doi: 10.1007/s00239-004-0046-3
2. Makarova KS, Grishin NV, Shabalina SA, et al. A putative RNA-interference-based immune system in prokaryotes: Computational analysis of the predicted enzymatic machinery, functional analogies with eukaryotic RNAi, and hypothetical mechanisms of action. Biol Direct 2006;1:7; doi: 10.1186/1745-6150-1-7
3. Bolotin A, Quinquis B, Sorokin A, et al. Clustered regularly interspaced short palindrome repeats (CRISPRs) have spacers of extrachromosomal origin. Microbiology 2005;151(Pt 8):2551–2561; doi: 10.1099/mic.0.28048-0
4. Gleditzsch D, Pausch P, Müller-Esparza H, et al. PAM identification by CRISPR-Cas effector complexes: Diversified mechanisms and structures. RNA Biol 2019;16(4):504–517; doi: 10.1080/15476286.2018.1504546
5. Newsom S, Parameshwaran HP, Martin L, et al. The CRISPR-Cas mechanism for adaptive immunity and alternate bacterial functions fuels diverse biotechnologies. Front Cell Infect Microbiol 2020;10:619763; doi: 10.3389/fcimb.2020.619763
6. Makarova KS, Wolf YI, Iranzo J, et al. Evolutionary classification of CRISPR-Cas systems: A burst of class 2 and derived variants. Nat Rev Microbiol 2020;18(2):67–83; doi: 10.1038/s41579-019-0299-x

7. Jinek M, Chylinski K, Fonfara I, et al. A programmable dual-RNA-guided DNA endonuclease in adaptive bacterial immunity. Science 2012;337(6096):816–821; doi: 10.1126/science.1225829
8. Nishimasu H, Ran FA, Hsu PD, et al. Crystal structure of Cas9 in complex with guide RNA and target DNA. Cell 2014;156(5):935–949; doi: 10.1016/j.cell.2014.02.001
9. Jiang F, Doudna JA. CRISPR-Cas9 structures and mechanisms. Annu Rev Biophys 2017;46:505–529; doi: 10.1146/annurev-biophys-062215-010822
10. Jinek M, Jiang F, Taylor DW, et al. Structures of Cas9 endonucleases reveal RNA-mediated conformational activation. Science 2014;343(6176):1247997; doi: 10.1126/science.1247997
11. Sternberg SH, Redding S, Jinek M, et al. DNA interrogation by the CRISPR RNA-guided endonuclease Cas9. Nature 2014;507(7490):62–67; doi: 10.1038/nature13011
12. Jiang F, Taylor DW, Chen JS, et al. Structures of a CRISPR-Cas9 R-loop complex primed for DNA cleavage. Science 2016;351(6275):867–871; doi: 10.1126/science.aad8282
13. Jiang F, Zhou K, Ma L, et al. Structural biology. A Cas9-guide RNA complex preorganized for target DNA recognition. Science 2015;348(6242):1477–1481; doi: 10.1126/science.aab1452
14. Sternberg SH, LaFrance B, Kaplan M, et al. Conformational control of DNA target cleavage by CRISPR-Cas9. Nature 2015;527(7576):110–113; doi: 10.1038/nature15544
15. Josephs EA, Kocak DD, Fitzgibbon CJ, et al. Structure and specificity of the RNA-guided endonuclease Cas9 during DNA interrogation, target binding and cleavage. Nucleic Acids Res 2016;44(5):2474; doi: 10.1093/nar/gkv1293
16. Raper AT, Stephenson AA, Suo Z. Functional insights revealed by the kinetic mechanism of CRISPR/Cas9. J Am Chem Soc 2018;140(8):2971–2984; doi: 10.1021/jacs.7b13047
17. Gong SZ, Yu HH, Johnson KA, et al. DNA unwinding is the primary determinant of CRISPR-Cas9 activity. Cell Rep 2018;22(2):359–371; doi: 10.1016/j.celrep.2017.12.041
18. Babu K, Kathiresan V, Kumari P, et al. Coordinated actions of Cas9 HNH and RuvC nuclease domains are regulated by the bridge helix and the target DNA sequence. Biochemistry 2021;60(49):3783–3800; doi: 10.1021/acs.biochem.1c00354
19. Casalino L, Nierzwicki L, Jinek M, et al. Catalytic mechanism of non-target DNA cleavage in CRISPR-Cas9 revealed by ab initio molecular dynamics. ACS Catal 2020;10(22):13596–13605; doi: 10.1021/acscatal.0c03566
20. East KW, Newton JC, Morzan UN, et al. Allosteric motions of the CRISPR-Cas9 HNH nuclease probed by NMR and molecular dynamics. J Am Chem Soc 2020;142(3):1348–1358; doi: 10.1021/jacs.9b10521
21. Nierzwicki L, Arantes PR, Saha A, et al. Establishing the allosteric mechanism in CRISPR-Cas9. Wiley Interdiscip Rev Comput Mol Sci 2021;11(3):e1503; doi: 10.1002/wcms.1503
22. Palermo G. Structure and dynamics of the CRISPR-Cas9 catalytic complex. J Chem Inf Model 2019;59(5):2394–2406; doi: 10.1021/acs.jcim.8b00988
23. Palermo G, Ricci CG, Fernando A, et al. Protospacer adjacent motif-induced allostery activates CRISPR-Cas9. J Am Chem Soc 2017;139(45):16028–16031; doi: 10.1021/jacs.7b05313
24. Zuo Z, Liu J. Allosteric regulation of CRISPR-Cas9 for DNA-targeting and cleavage. Curr Opin Struct Biol 2020;62:166–174; doi: 10.1016/j.sbi.2020.01.013
25. Sundaresan R, Parameshwaran HP, Yogesha SD, et al. RNA-independent DNA Cleavage Activities of Cas9 and Cas12a. Cell Rep 2017;21(13):3728–3739; doi: 10.1016/j.celrep.2017.11.100
26. Saha C, Mohanraju P, Stubbs A, et al. Guide-free Cas9 from pathogenic *Campylobacter jejuni* bacteria causes severe damage to DNA. Sci Adv 2020;6(25):eaaz4849; doi: 10.1126/sciadv.aaz4849
27. Li B, Yan J, Zhang Y, et al. CRISPR-Cas12a possesses unconventional DNase activity that can be inactivated by synthetic oligonucleotides. Mol Ther Nucleic Acids 2020;19:1043–1052; doi: 10.1016/j.omtn.2019.12.038
28. Saha C, Horst-Kreft D, Kross I, et al. *Campylobacter jejuni* Cas9 modulates the transcriptome in Caco-2 intestinal epithelial cells. Genes (Basel) 2020;11(10):1193; doi: 10.3390/genes11101193
29. Slaymaker IM, Gao L, Zetsche B, et al. Rationally engineered Cas9 nucleases with improved specificity. Science 2016;351(6268):84–88; doi: 10.1126/science.aad5227
30. Tang H, Yuan H, Du W, et al. Active-site models of *Streptococcus pyogenes* Cas9 in DNA cleavage state. Front Mol Biosci 2021;8:653262; doi: 10.3389/fmolb.2021.653262
31. Babu K, Amrani N, Jiang W, et al. Bridge helix of Cas9 modulates target DNA cleavage and mismatch tolerance. Biochemistry 2019;58(14):1905–1917; doi: 10.1021/acs.biochem.8b01241
32. Schneider CA, Rasband WS, Eliceiri KW. NIH Image to ImageJ: 25 Years of image analysis. Nat Methods 2012;9(7):671–675.
33. Chen. Multiple Curve Fitting with Common Parameters Using NLINFIT. MATLAB Central File Exchange. Available from: https://www.mathworks.com/matlabcentral/fileexchange/40613-multiple-curve-fitting-with-common-parameters-using-nlinfit [Last accessed: September 6, 2023].
34. Palermo G, Miao Y, Walker RC, et al. Striking plasticity of CRISPR-Cas9 and key role of non-target DNA, as revealed by molecular simulations. ACS Cent Sci 2016;2(10):756–763; doi: 10.1021/acscentsci.6b00218
35. Zuo Z, Liu J. Cas9-catalyzed DNA cleavage generates staggered ends: Evidence from molecular dynamics simulations. Sci Rep 2016;5:37584; doi: 10.1038/srep37584
36. Kuscu C, Arslan S, Singh R, et al. Genome-wide analysis reveals characteristics of off-target sites bound by the Cas9 endonuclease. Nat Biotechnol 2014;32(7):677–683; doi: 10.1038/nbt.2916
37. Grotz KK, Cruz-León S, Schwierz N. Optimized magnesium force field parameters for biomolecular simulations with accurate solvation, ion-binding, and water-exchange properties. J Chem Theory Comput 2021;17(4):2530–2540; doi: 10.1021/acs.jctc.0c01281
38. Grotz KK, Schwierz N. Magnesium force fields for OPC water with accurate solvation, ion-binding, and water-exchange properties: Successful transfer from SPC/E. J Chem Phys 2022;156(11):114501; doi: 10.1063/5.0087292
39. Furuhata Y, Kato Y. Asymmetric roles of two histidine residues in *Streptococcus pyogenes* Cas9 catalytic domains upon chemical rescue. Biochemistry 2021;60(3):194–200; doi: 10.1021/acs.biochem.0c00766
40. Deweese JE, Osheroff N. The use of divalent metal ions by type II topoisomerases. Metallomics 2010;2(7):450–459; doi: 10.1039/c003759a
41. Irving H, Williams R. Order of stability of metal complexes. Nature 1948;162:746–747; doi: 10.1038/162746a0
42. Dürr SL, Bohuszewicz O, Suardiaz R, et al. The dual role of histidine as general base and recruiter of a third metal ion in HIV-1 RNase H. ChemRxiv; 2019.
43. Chen JS, Ma E, Harrington LB, et al. CRISPR-Cas12a target binding unleashes indiscriminate single-stranded DNase activity. Science 2018;360(6387):436–439; doi: 10.1126/science.aar6245
44. Swarts DC, Jinek M. Mechanistic insights into the cis- and trans-acting DNase activities of Cas12a. Mol Cell 2019;73(3):589.e4–600.e4; doi: 10.1016/j.molcel.2018.11.021

Received: April 7, 2023
Accepted: November 10, 2023
Online Publication Date: December 15, 2023

Supplementary Information

Differential divalent metal binding by SpyCas9's RuvC active site contributes to non-specific DNA cleavage

Sydney N. Newsom,[1#] Duen-Shian Wang,[2#] Saadi Rostami,[1] Isabelle Schuster,[3] Hari Priya Parameshwaran,[1] Yadin G. Joseph,[1] Peter Z. Qin,[3] Jin Liu,[2*] Rakhi Rajan.[1*]

[1]Department of Chemistry and Biochemistry, Price Family Foundation Institute of Structural Biology, Stephenson Life Sciences Research Center, University of Oklahoma, 101 Stephenson Parkway, Norman, OK, 73019, USA

[2]Department of Pharmaceutical Sciences, University of North Texas System College of Pharmacy, University of North Texas Health Science Center, 3500 Camp Bowie Blvd, Fort Worth, TX, 76107, USA

[3] Department of Chemistry, University of Southern California, 3430 S. Vermont Ave., Los Angeles, CA, 90089, USA

# These authors contribute equally

*Correspondence: r-rajan@ou.edu; jin.liu@unthsc.edu

Table of Contents

Supplementary Materials and Method

1. Protein purification

The purification procedure closely adhered to previously documented methods.[1,2] Rosetta (DE3) cells were cultured in 2XYT medium at 37°C to reach the optical density (OD) of 0.8 at 600 nm. Subsequently, the cells were induced with 0.2 mM Isopropyl-ß-D-thiogalactopyranoside (IPTG) and allowed to incubate at 18°C for 16 hours. Cells were harvested, and then resuspended in a buffer composed of 50 mM TRIS (pH 8), 500 mM NaCl, 5 mM imidazole, and 1 mM TCEP, in preparation for Nickel nitrilotriacetic acid (Ni-NTA) chromatography.

To ensure protein integrity, we supplemented the thawed cells with protease inhibitors, including pepstatin (1µg/mL), leupeptin (1µg/mL), benzimidine (1mM), and phenylmethylsulfonyl fluoride (PMSF, 1mM), and subsequently lysed them using a sonicator. The lysate was then centrifuged at 18,000 rpm for 45 minutes and the supernatant was loaded onto a Ni-NTA column. Protein fractions were subsequently eluted using a continuous gradient elution with a buffer composed of 50 mM TRIS (pH 8), 500 mM NaCl, 500 mM imidazole, and 1 mM TCEP. SpyCas9 protein fractions were collected and the MBP tag was cleaved by incubating with TEV (Tobacco etch virus) protease[3] at 4°C overnight while concurrently dialyzing into a Cation exchange column (SP HP) equilibration buffer containing 20 mM HEPES (pH 7.5), 150 mM KCl, 2 mM DTT, and 10% glycerol. After dialysis, the sample was loaded onto the equilibrated SP HP column, and protein was eluted through a continuous salt gradient using elution buffer (20 mM HEPES, pH 7.5, 1 M KCl, 2 mM DTT, and 10% glycerol). Fractions were combined and concentrated to a volume of approximately 2 mL, then loaded into an equilibrated HiPrep^{TM} Sephacryl S300 column for further purification. The elution was performed using a buffer consisting of 20 mM HEPES (pH 7.5), 150 mM KCl, and 2 mM TCEP. Subsequently, pure fractions were collected and further concentrated and rapidly frozen using liquid nitrogen, and stored at -80°C.[1,2]

2. *In vitro* SpyCas9 activity assays

A. Guide RNA-free single-stranded M13mp18 DNA cleavage:

Unless otherwise stated, reaction components contained 1X buffer (20 mM HEPES pH 7.5, 150 mM KCl, 2 mM TCEP), 100 ng (~4.5 nM) single stranded plasmid DNA (M13mp18, NEB, N4040S), 10 mM divalent metal, and 100 nM SpyCas9. Reactions were performed at 37°C for the desired time points. All divalent metals had chloride counterions. Since we noticed accumulation of reaction products in the wells of the gels when the assay contained Co^{2+}, Co^{2+} reactions were stopped with a 5X stock of 50 mM EDTA and 75 mM $CaCl_2$ (for Proteinase K activity) and treated with 0.8 Units of Proteinase K (New England Biolabs) for 20 min at 50°C. All

the reactions were prepared for agarose gel electrophoresis by adding 2X stop dye (100 mM EDTA, 2% SDS, 20% glycerol, and 0.08% Orange G dye). The reaction products were resolved on a 1% agarose gel and the bands were visualized post-gel running using 0.1 µg/mL ethidium bromide. Three replications were done for SpyCas9^{H982A} and SpyCas9^{WT} using two independent protein preparations each.

B. *gRNA-dependent* double-stranded pUC19 DNA cleavage:

Reaction components were 1X cleavage buffer (20 mM Tris pH 7.5, 100 mM KCl, 5% (v/v) glycerol and 0.5 mM TCEP), 100 ng (~5 nM) double stranded plasmid DNA (pUC19) containing a target site complementary to the guide region of the sgRNA (for time-course assays) or with some mismatches to the guide region (for off-target DNA cleavage assays), 10 mM divalent metal, 120 nM sgRNA, and 100 nM SpyCas9 incubated at 37°C for 15 min unless otherwise stated. Two sets of reactions were performed, one without and the other with preincubation of Cas9 and sgRNA (37°C for 15 min). The reaction products were resolved on a 1.1% agarose gel and the bands were visualized post-gel running using 0.1 µg/mL ethidium bromide. Four replications were done for SpyCas9^{H982A} and SpyCas9^{WT} using two independent protein preparations each.

C. gRNA-dependent double-stranded oligo DNA cleavage:

Oligo DNAs with and without 5' 6-FAM (Fluorescein) labeling were annealed using 1X annealing buffer (30 mM HEPES pH 7.5 and 10 mM Potassium Acetate) to form a 54-base pair DNA substrate with 6-FAM labeling on either the TS or the NTS strand. The reaction components included 1X cleavage buffer (20 mM Tris pH 7.5, 100 mM KCl, 5% (v/v) glycerol, and 10 mM $MgCl_2$), approximately 10 nM of the annealed DNA, 250 nM sgRNA, and 250 nM SpyCas9. A preincubation step was performed by incubating sgRNA and Cas9 at 37°C for 15 minutes to enable binary complex formation, followed by addition of DNA. The reaction was stopped at the indicated time points with a stop dye (1X composition: 10 mM EDTA, 47% Formamide, and 1% SDS). Samples were then resolved on a 16% denaturing urea-acrylamide gel and were visualized using a Bio-Rad ChemiDoc MP CCD Imaging System using fluorescence with 490 nm excitation.

3. Procedure of MD simulations

A. Preparations for all MD simulations

The structures selected for MD simulations (see Section 5A of Materials and Methods) were solvated in truncated octahedral boxes of TIP3P waters with a minimal thickness of 13 Å from each edge

using tLEaP of Ambertools 16.[4] The system was neutralized by Cl^-, and additional K^+ and Cl^- were added to achieve the physiological ionic condition of 150 mM. Additional Mg^{2+}/Mn^{2+} ions were added to reach 5 mM of Mg^{2+}/Mn^{2+} concentration. Adding the additional 10 Mg^{2+}/Mn^{2+} ions in the ion-perturbation model increased the Mg^{2+}/Mn^{2+} concentration to 8.6 mM. In all simulations of SpyCas9- NTS-DNA and the ion-perturbation of SpyCas9- NTS-DNA models, Mg^{2+}/Mn^{2+} ions did not form specific interactions with any atoms of SpyCas9 or NTS-DNA (data not shown) other than the catalytic site, implying our simulations were less likely biased by other Mg^{2+}/Mn^{2+} ions in the system.

The system applied the amber force fields ff14SB[5] for protein, OL15[6] for DNA , TIP3P[7] for waters, the Joung-Cheatham parameter sets[8] for monovalent ions (K^+, Cl^-) and the optimized IOD-LJ parameter set[9] for Mg^{2+}/Mn^{2+}**.** The CPPTRAJ program in Amber Tools[10] was utilized to randomize the positions of K^+ and Cl^- such that the randomized ions were at least 4 Å away from any protein or DNA atom, eliminating the bias from monovalent ion-protein and monovalent ion-DNA interactions during the MD simulations.

B. Protocols for all Molecular Dynamics simulations

All systems underwent a sequence of steps to reach equilibration as described in our previous work.[11] First, the system was subjected to energy minimization, followed by slow heating from 0 K to the target of 310.15 K in an isothermal isochoric (NVT) ensemble, while the heavy atoms were restrained with the same force constant. 1 ns equilibration was performed in the isothermal-isobaric (NPT) condition with the weaker heavy atoms constrained (force constant for restraint: 1.0). Further, Mg^{2+}/Mn^{2+} ions in both the HNH and RuvC domains received additional constraint in the equilibration process. Finally, the simulation was performed under the NPT ensemble without restraints, extending up to 500 ns. The pressure was controlled at 1.013 bar *via* the Monte Carlo barostat, and the temperature was maintained at 310.15 K through the Langevin thermostat implemented in AMBER16. The bonds involving hydrogens were constrained by the SHAKE algorithm[12] with 2 fs integration steps during the heating, equilibration and production stages. Hydrogen mass repartitioning[13,14] was used to facilitate a 4 fs-time step in MD production. For each setting, three individual 500 ns MD simulations were conducted. The first 100 ns of each trajectory of all simulations was considered as the equilibration and discarded based on RMSD analysis (Figures S13 and S14). All simulations were performed by the CUDA-accelerated version of AMBER16 pmemd engine.[15]

4. Free energy of binding estimations (MM/GBSA and MM/PBSA)

A. MM/GBSA for free energy of NTS-DNA binding to SpyCas9

The free energy of NTS-DNA binding to SpyCas9 was estimated *via* the end-point molecular mechanics generalized Born surface area (MM/GBSA) approach.[16,17] The MM/GBSA calculations were done with the program MMPBSA.py in AmberTools16.[16] Before calculations, water, K^+, Cl^- and Mg^{2+}/Mn^{2+} were stripped. NTS-DNA was regarded as the ligand, and SpyCas9 was set as the receptor. MM/GBSA calculations were performed on 3000 snapshots accumulated from 200-300 ns production trajectories of 3 individual runs evenly with a time interval of 100 ps on SpyCas9^{WT}- NTS-DNA-Mg^{2+}, SpyCas9^{WT}- NTS-DNA-Mn^{2+}or SpyCas9^{H982A}- NTS-DNA-Mn^{2+}.

B. MM/PBSA for free energy of Mg^{2+}_A/Mn^{2+}_A binding to SpyCas9+ NTS-DNA complex

The free energy of Mg^{2+}_A/Mn^{2+}_A binding at the RuvC catalytic center was estimated *via* the alternative molecular mechanics-Poisson−Boltzmann surface area (MM/PBSA),[18] and MMPBSA.py program in AmberTools16 was applied.[16] Before calculations, water, K^+, Cl^- and non-catalytic Mg^{2+}/Mn^{2+} were stripped, and only three catalytic Mg^{2+}/Mn^{2+} (one for the HNH center and two for the RuvC center) were kept. The perturbed ion (Mg^{2+}_A/Mn^{2+}_A) was regarded as ligand, and SpyCas9- NTS-DNA-Mg^{2+}/Mn^{2+}(HNH)-Mg^{2+}_B/Mn^{2+}_B (RuvC) was set as receptor. MM/PBSA calculations were performed on 250 snapshots from 450-500 ns production trajectories (S1 run from SpyCas9^{WT}- NTS-DNA-Mg^{2+}, S3 from SpyCas9^{WT}- NTS-DNA-Mn^{2+}) (Table S2).

5. Other data analyses

The CPPTRAJ program in Amber Tools[10] was utilized for atomic distance analysis and contact estimations between SpyCas9 and NTS-DNA. XMGRACE was applied for plotting.[19] The mass-weight heavy atom RMSD was utilized to evaluate structure relaxation in all the simulations. For all simulations, steep changes in RMSD were observed during the 1-50 ns simulation time-frame. After structure relaxation, 100-500 ns trajectories of all simulations were utilized for data analysis according to RMSD evaluation (Figures S13 and S14). All computational analyses are summarized in Table S3.

Predicting which SpyCas9 residues contribute to gRNA-free DNA cleavage

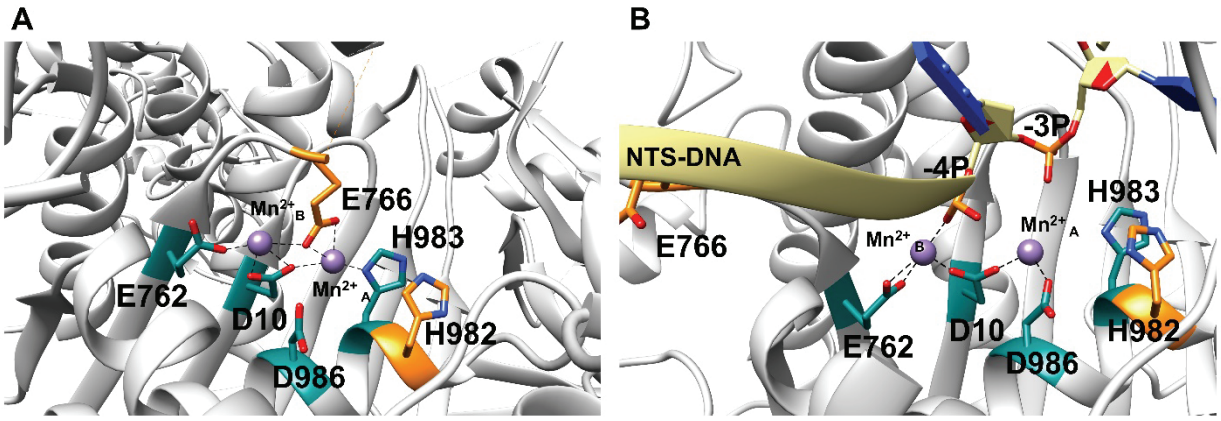

Figure S1. RuvC nuclease active site. (A) RuvC catalytic site in apo SpyCas9 (PDB ID: 4CMQ).[20] Catalytic residues essential for gRNA-dependent DNA cleavage (D10, E762, H983, and D986 colored in dark cyan) are shown among non-essential residue E766 and H982 colored in orange. **(B)** Mn^{2+} coordination by the non-target DNA strand (NTS-DNA colored as khaki) and catalytic residues in the absence of gRNA. The catalytic residues are shown among non-essential residue E766 and H982. This figure is generated from MD simulation created structure after 500 ns simulation.

SpyCas9 variants with amino acid substitutions in the RuvC active site assayed for gRNA-free and gRNA-dependent DNA cleavage activities.

The E766A substitution in SpyCas9 (SpyCas9^{E766A}) does not remove the undesired gRNA-free cleavage activity since this variant degrades single stranded M13mp18 DNA in 30 s with 10 mM Mn^{2+} in the absence of gRNA (Figure S2A). Figure S2D shows that the wild type SpyCas9 (SpyCas9^{WT}) can linearize >80% of the double stranded pUC19 substrate DNA *via* gRNA-dependent cleavage in less than 5 min, but SpyCas9^{E766A} takes ~15 min to achieve this. Figure S2B shows that H982A has negligible gRNA-free DNA cleavage activity with 10 mM Mn^{2+}, and Figure S2E shows that H982A is active for gRNA-dependent DNA cleavage with 100% nicking and ~50% linearization of the substrate after an hour of incubation. The double variant SpyCas9$^{E766A/H982A}$ has reduced gRNA-free DNA cleavage activity equal to that of SpyCas9^{H982A} (Figures S2B and S2C), but it also has reduced gRNA-dependent DNA cleavage activity compared to H982A alone (a larger amount of nicked product in all time points in the double variant compared to SpyCas9^{H982}) (Figures S2E and S2F). This indicates that H982 contributes to gRNA-free DNA cleavage activity more that E766 does, and that simultaneous substitution of E766 and H982 to Ala reduces gRNA-dependent DNA cleavage. The H983A mutation removes both gRNA-dependent and gRNA-free DNA cleavage activities (Figure S2G). Overall, the single H982A substitution (SpyCas9^{H982A}) has the best reduction in gRNA-free DNA cleavage and maintenance of the desirable gRNA-dependent DNA cleavage activity.

The protein and metal titration assays show that gRNA-free ssDNA cleavage activity with Mn^{2+} is protein and metal concentration dependent (Figures S2 – S5). The protein concentration carried forward for time-course assays was 100 nM, but there is ssDNA cleavage at 20 nM and 50 nM of protein concentrations (Figure S3).

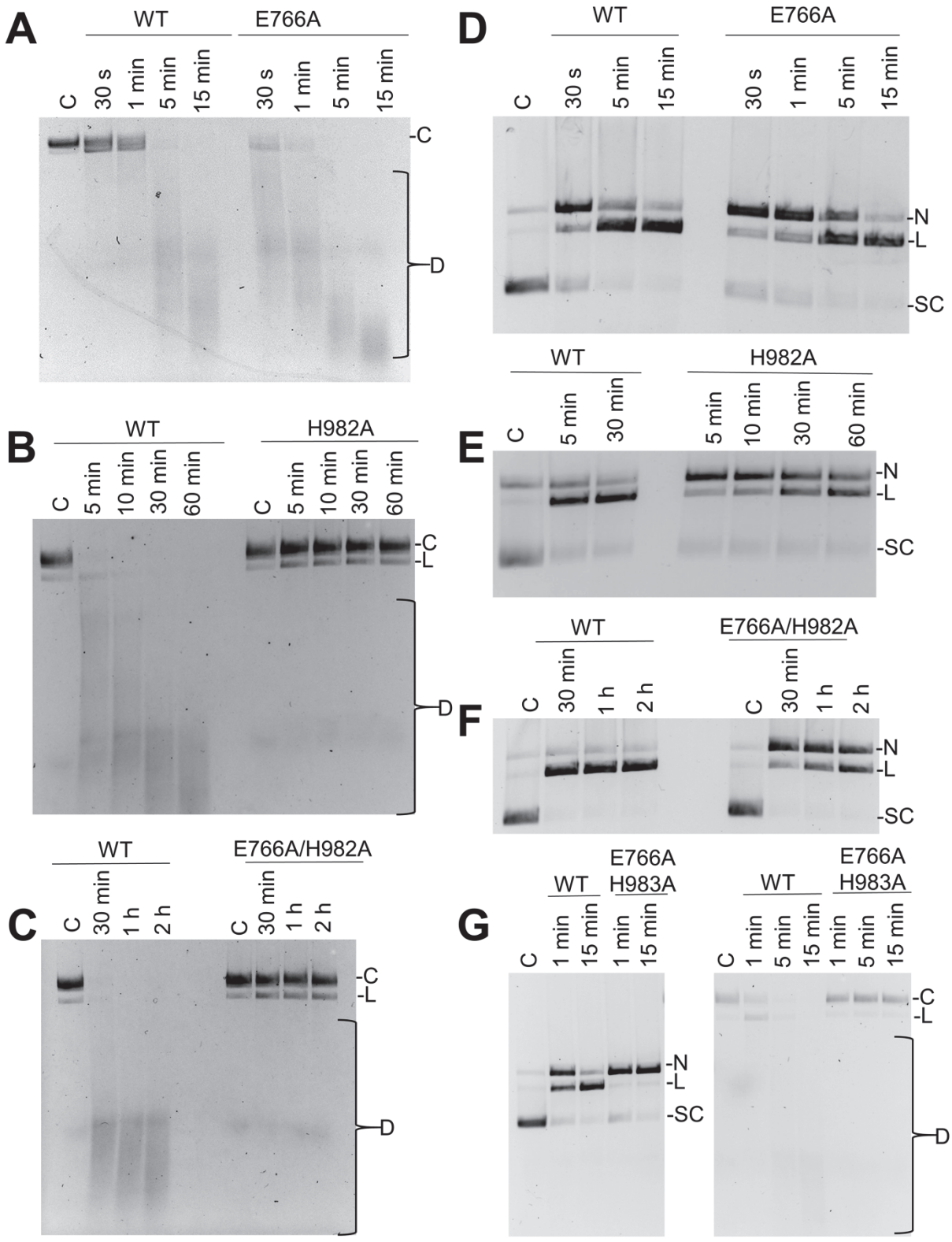
A
WT
E766A
C
30 s
1 min
5 min
15 min
30 s
1 min
5 min
15 min
C
D
B
WT
H982A
C
5 min
10 min
30 min
60 min
C
5 min
10 min
30 min
60 min
C
L
D
C
WT
E766A/H982A
C
30 min
1 h
2 h
C
30 min
1 h
2 h
C
L
D
D
WT
E766A
C
30 s
5 min
15 min
30 s
1 min
5 min
15 min
N
L
SC
E
WT
H982A
C
5 min
30 min
5 min
10 min
30 min
60 min
N
L
SC
F
WT
E766A/H982A
C
30 min
1 h
2 h
C
30 min
1 h
2 h
N
L
SC
G
WT
E766A
H983A
C
1 min
15 min
1 min
15 min
WT
E766A
H983A
C
1 min
5 min
15 min
1 min
5 min
15 min
N
L
SC
C
L
D

Figure S2. Characterizing different RuvC active site variants of SpyCas9 for their ability to promote gRNA-free DNA cleavage. DNA cleavage time-course assays for **(A)** SpyCas9^{WT} and SpyCas9^{E766A} gRNA-free cleavage of single stranded DNA plasmid (M13mp18), **(B)** SpyCas9^{WT} and SpyCas9^{H982A} gRNA-free cleavage of M13mp18, **(C)** SpyCas9^{WT} and SpyCas9$^{E766A/H982A}$ double variant gRNA-free cleavage of M13mp18, **(D)** SpyCas9^{WT} and SpyCas9^{E766A} gRNA-dependent cleavage of double stranded DNA plasmid (pUC19), **(E)** SpyCas9^{WT} and SpyCas9^{H982A} gRNA-dependent cleavage of pUC19, **(F)** SpyCas9^{WT} and SpyCas9$^{E766A/H982A}$ double variant gRNA-dependent cleavage of pUC19, and **(G)** SpyCas9 $^{E766A/H983A}$ gRNA-dependent cleavage of pUC19 (left) and gRNA-free cleavage of M13mp18 (right). Only one protein preparation each was done for SpyCas9$^{E766/H983A}$, SpyCas9^{E766} and SpyCas9$^{E766/H982A}$. Protein concentration is 100 nM. gRNA-free DNA cleavage (panels A, B, C, and G) was done with 10 mM Mn^{2+}, and gRNA-dependent DNA cleavage (panels D, E, F, and G) was done with 10 mM Mg^{2+}. [C – circular, D – degraded, N – nicked, L – Linear, SC – supercoiled.]

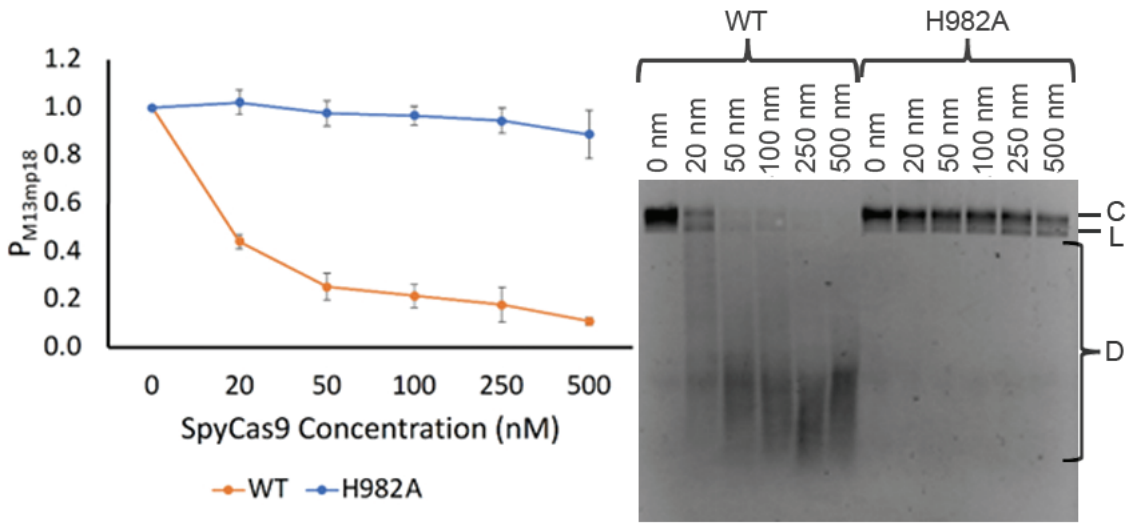

Figure S3. SpyCas9 protein concentration titration assay of gRNA-free ssDNA cleavage with Mn^{2+}. Reaction conditions were 10 mM Mn^{2+} and 100 ng M13mp18 ssDNA plasmid incubated for 30 min at 37°C. $P_{M13mp18}$ is the fraction of uncleaved DNA (Equation 1a). Error bars are the standard error of the mean (SEM) of three replications. A representative gel is shown to the right. [C – circular, L – linear, D – degraded.]

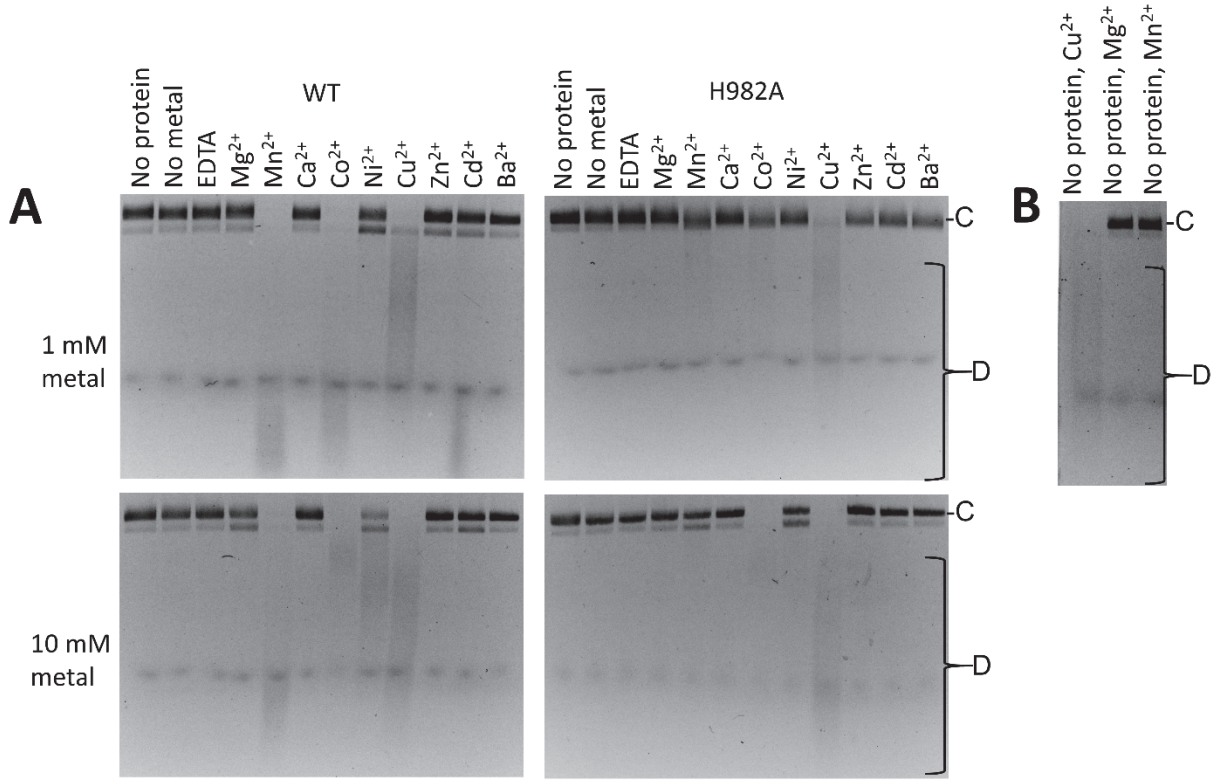

Figure S4. Analysis of the effect of different divalent metals on gRNA-free DNA cleavage. **(A)** Uncropped agarose gels (cropped gels are in main text Figure 1A) quantified to construct the bar graph in panel B of Figure 1. Only Mg^{2+}, Mn^{2+}, Co^{2+}, Ni^{2+} are shown in Figure 1, but the gels shown in this figure include additional metals: Cu^{2+}, which was found to degrade M13mp18 ssDNA without protein (data shown in panel S4B), and Ca^{2+}, Zn^{2+}, Cd^{2+}, and Ba^{2+}, which were not found to facilitate gRNA-free DNA cleavage. **(B)**. Protein-independent degradation of M13mp18 in the presence of Cu^{2+}. [C – circular, L – linear, D – degraded].

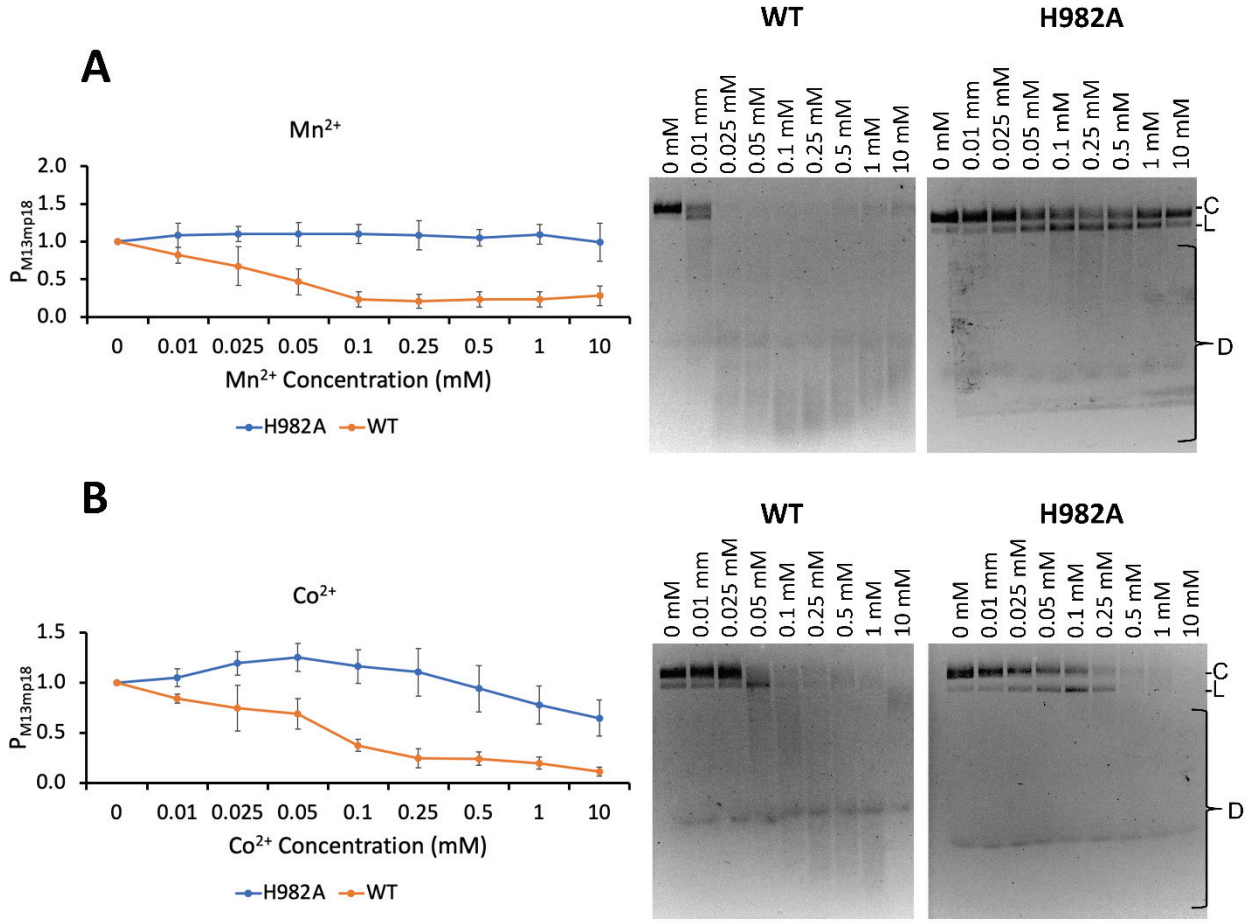

Figure S5. Divalent metal titration assay of SpyCas9 gRNA-free ssDNA cleavage. (A) Mn^{2+} and **(B)** Co^{2+}. Reaction conditions were 100 nM SpyCas9 and 100 ng M13mp18 ssDNA plasmid incubated for 30 min at 37°C. $P_{M13mp18}$ is the fraction of uncleaved DNA (Equation 1a). Error bars are the standard error of the mean (SEM) of three replications. Representative gels are shown to the right. [C – circular, L – linear, D – degraded.]

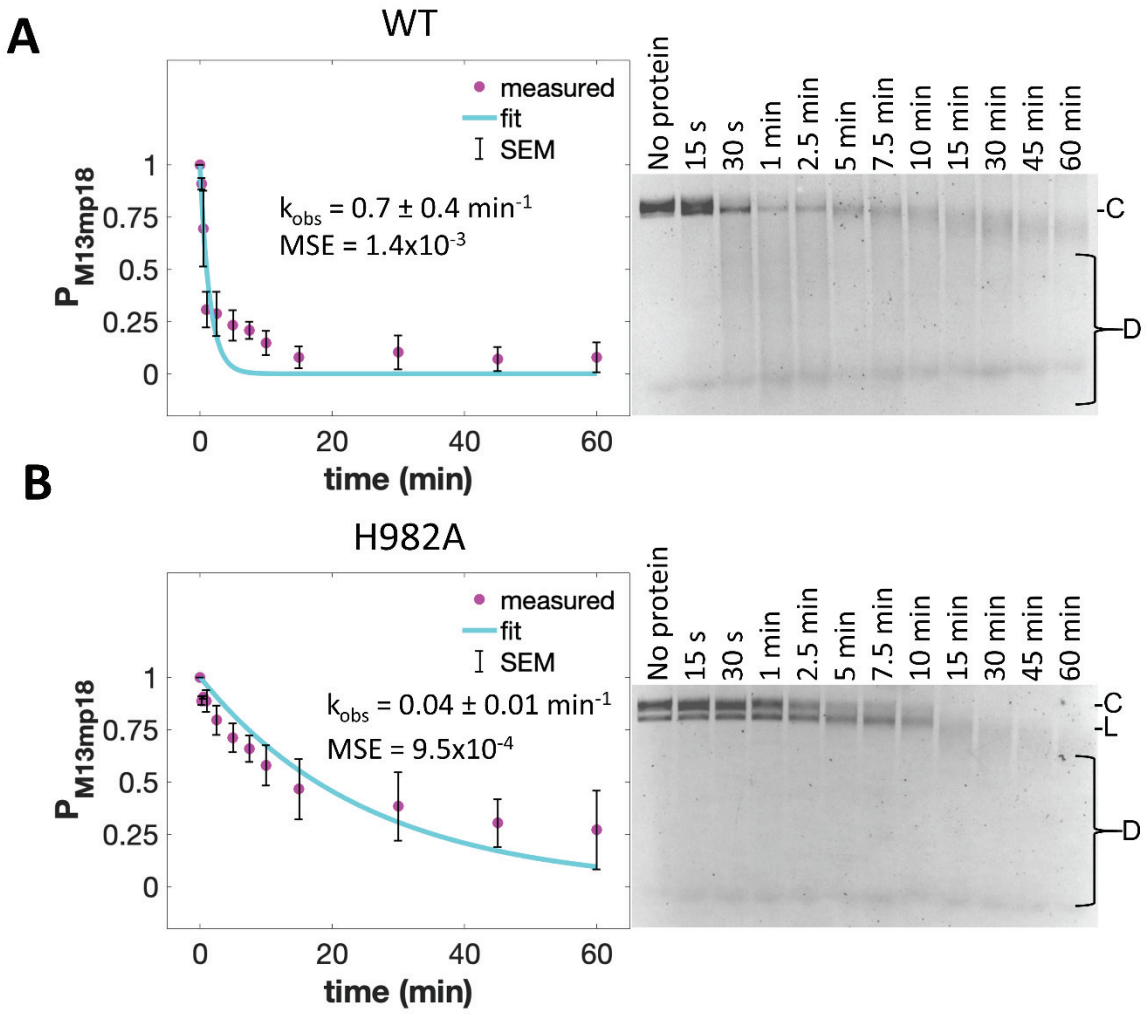

Figure S6. Determination of rate constant for SpyCas9 gRNA-free cleavage of circular, single stranded M13mp18 DNA in the presence of Co^{2+}. Single exponential fit (cyan line, Equation 1b) of average fraction of uncleaved DNA (Equation 1a, $P_{M13mp18}$) plotted against time (t, min) for **(A)** SpyCas9^{WT}-Co^{2+} and **(B)** SpyCas9^{H982A}-Co^{2+}. The data points (magenta) are the average of three replications with standard error of the mean (SEM) shown as error bars. Mean square error (MSE) represents deviation of data points from the single exponential fit line. The error reported for the rate constant (k_{obs}) is the 95% confidence interval determined with the MATLAB fitting program. [C – circular, L – linear, D – degraded.] Note that analyzing the data using double-exponential decay resulted in similar conclusions [data not shown].

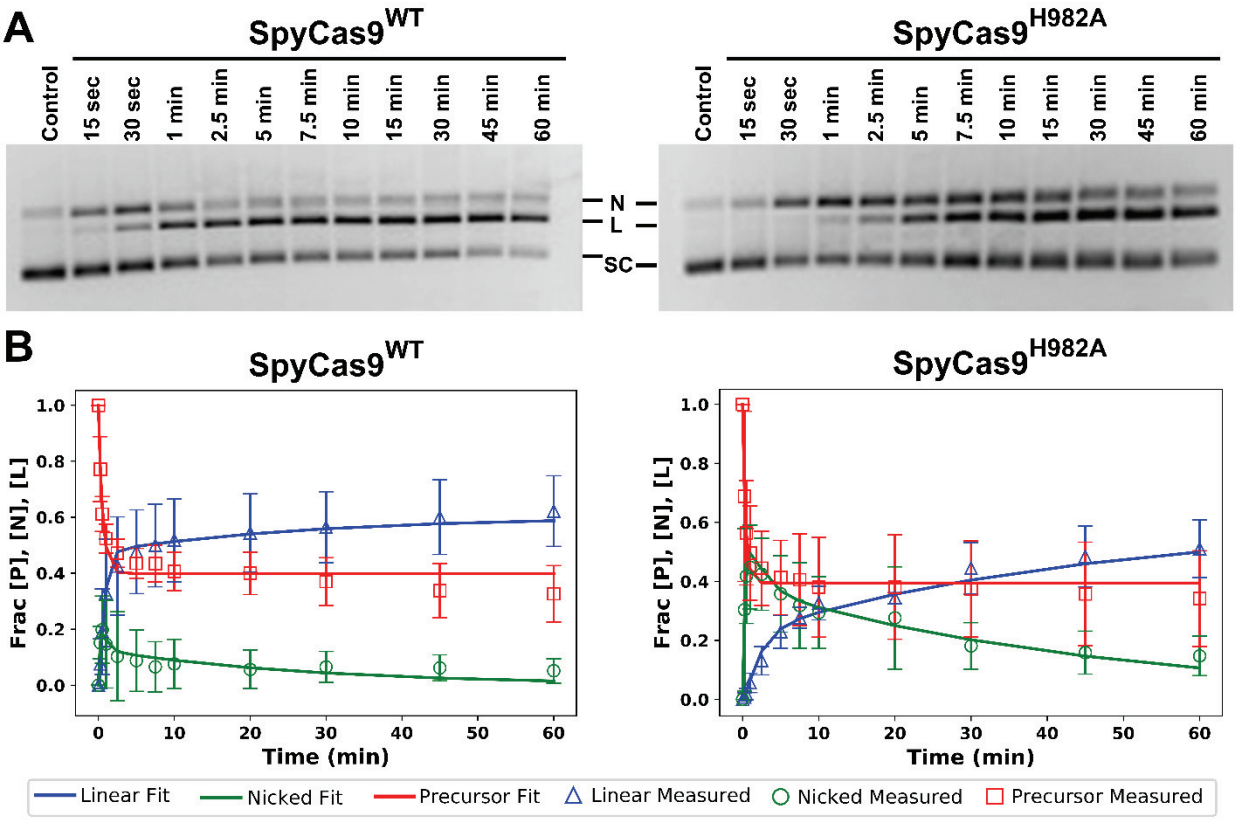

C

enzyme	Active fraction	$k_{1,HNH}$ (min^{-1})	$k_{2,RuvC}$ (min^{-1})	$k_{1,RuvC}$ (min^{-1})	$k_{2,HNH}$ (min^{-1})
SpyCas9^{WT}	0.60 ± 0.02	1.45 ± 0.25	3.93 ± 1.59	0.38 ± 0.12	0.04 ± 0.02
SpyCas9^{H982A}	0.61 ± 0.02	1.62 ± 0.45	0.02 ± 0.01	0.96 ± 0.33	0.50 ± 0.38

D

enzyme	$k_{1,HNH} + k_{1,RuvC}$	$k_{2,RuvC} / k_{1,HNH}$	$k_{2,HNH} / k_{1,RuvC}$
SpyCas9^{WT}	1.825	2.717	0.095
SpyCas9^{H982A}	2.581	0.013	0.516
SpyCas9^{H982A}/ SpyCas9^{WT} ratio	1.41	0.005	5.44

Figure S7. Assessment of gRNA-dependent DNA cleavage at 37°C without pre-incubation of Cas9 and gRNA to form the binary complex in the presence of Mg^{2+}. (A) Representative gels for gRNA-dependent DNA cleavage without preincubation of Cas9 and sgRNA. **(B)** Monitoring the amount of supercoiled, nicked, and linear DNA during the time course of gRNA-dependent DNA cleavage. **(C)** Rate constants for a parallel sequential DNA cleavage model for gRNA-dependent DNA cleavage by SpyCas9^{WT} and SpyCas9^{H982A}. **(D)** Comparison of the relative

efficiency of DNA cleavage and the use of TS and NTS pathways by SpyCas9^{WT} and SpyCas9^{H982A}. Similar to the pattern seen with preincubation, there is ~5-fold increase in the use of NTS pathway by SpyCas9^{H982A} to linearize DNA. The experiment was conducted at 37°C without pre-incubation of Cas9 and gRNA to form the binary complex.

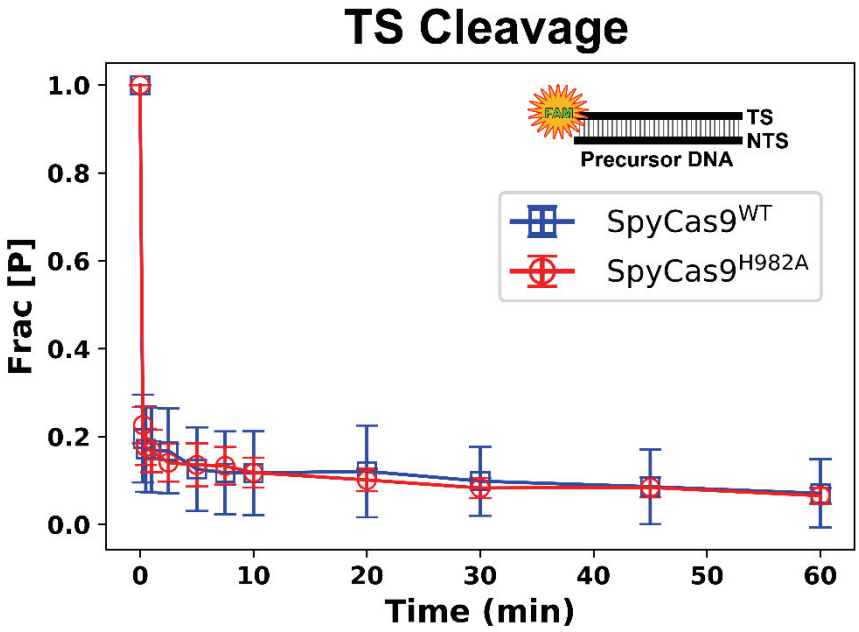

Figure S8. Assessment of TS cleavage by HNH using DNA oligo substrates. Oligo dsDNA (54-mer) was labeled at the 5'-end of TS by FAM and was used as a substrate for gRNA-dependent DNA cleavage in the presence of Mg^{2+}. The time traces of TS disappearance for $SpyCas9^{WT}$ and $SpyCas9^{H982A}$ overlap with each other, indicating no differences in the activity of HNH that can be detected by this measurement.

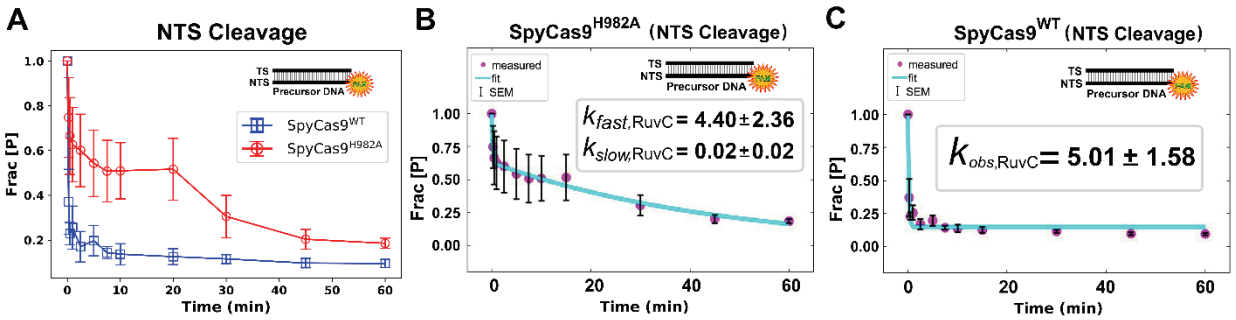

Figure S9. Assessment of NTS cleavage by RuvC using DNA oligo substrates. Oligo dsDNA (54-mer) was labeled at the 5'-end of NTS by FAM was used as a substrate for gRNA-dependent DNA cleavage. **(A)** Overlay of time traces shows RuvC activity differs between SpyCas9^{WT} and SpyCas9^{H982A}. **(B)** Fitting of SpyCas9^{H982A} NTS cleavage requires a bi-exponential decay. Note that the two rate constants obtained differ by more than 10 times. This is consistent with the plasmid cleavage yielding very different $k_{1,RuvC}$ (0.59 min^{-1}) and $k_{2,RuvC}$ (0.02 min^{-1}) for SpyCas9^{H982A} (Table 2, main text). **(C)** SpyCas9^{WT} NTS cleavage data is sufficiently fit to a single exponential decay. Note that from plasmid cleavage $k_{1,RuvC}$ (0.74 min^{-1}) and $k_{2,RuvC}$ (2.25 min^{-1}) differ less than 10 times. This smaller difference is consistent with the lack of an apparent bi-phasic decay observed in the oligo cleavage data.

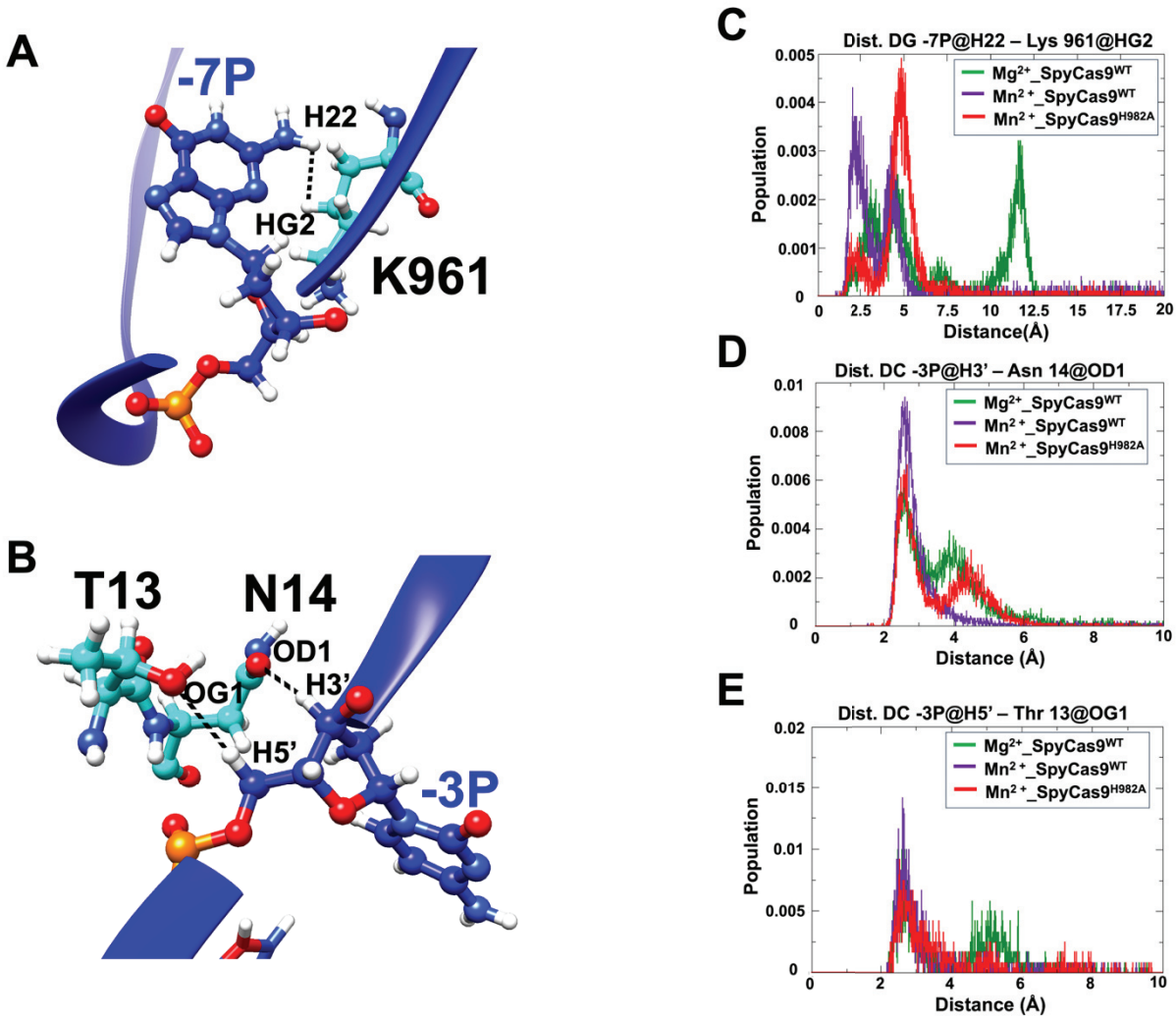

Figure S10. Distance analysis comparing the interactions stabilizing NTS-DNA binding with SpyCas9^{WT} versus SpyCas9^{H982A}. (A, B) An enlarged view of the black-colored circles from Figure 5A. **(C to E)** Distance distribution of the interactions between DG -7P@H22 – Lys 961@HG2, DC -3P@OH3' – Asn 14@OD1, and DC -3P@H5' – Thr 13@OG1, respectively. [100-400 ns; accumulated 12000 frames]**.**

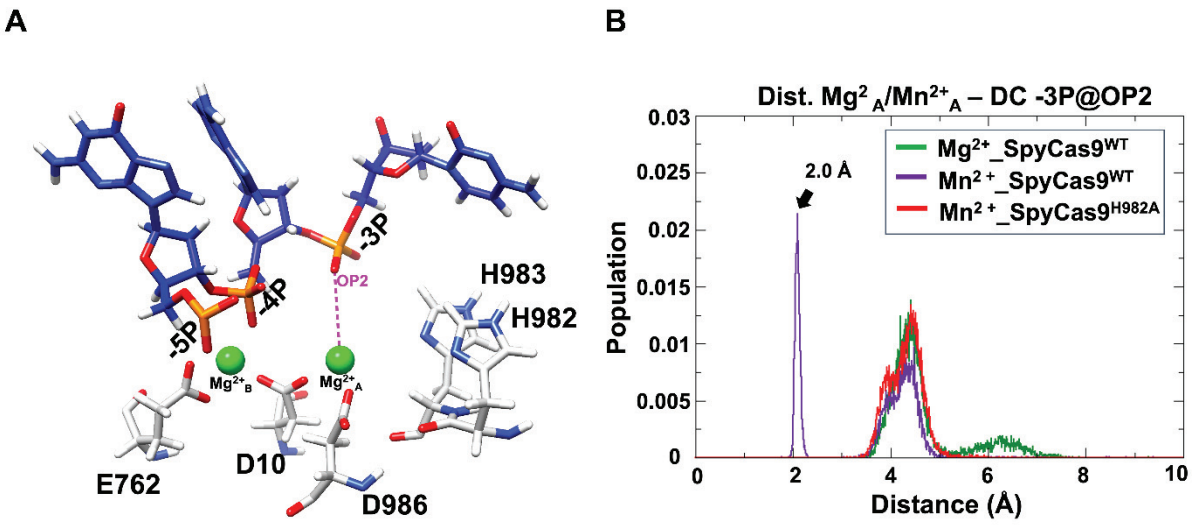

Figure S11. The distance between $Mg^{2+}A$/$Mn^{2+}A$ and non-target DNA (NTS-DNA) DC -3P (@OP2) in simulations. (A) Scheme of the distance between $Mg^{2+}A$ and NTS-DNA (-3P) in our structural model for $SpyCas9^{WT}$ (before perturbing the divalent metal ions). The dashed magenta line denotes the distance. **(B)** Distance distribution of the interactions between $Mg^{2+}A$ /$Mn^{2+}A$ and NTS-DNA DC -3P (@OP2). [100-400 ns; accumulated 12000 frames]**.** Mn^{2+}_A, not Mg^{2+}_A, maintains a close interaction with the scissile phosphate during the simulation timeline in $SpyCas9^{WT}$, while this interaction is lost in $SpyCas9^{H982A}$-Mn^{2+}_A.

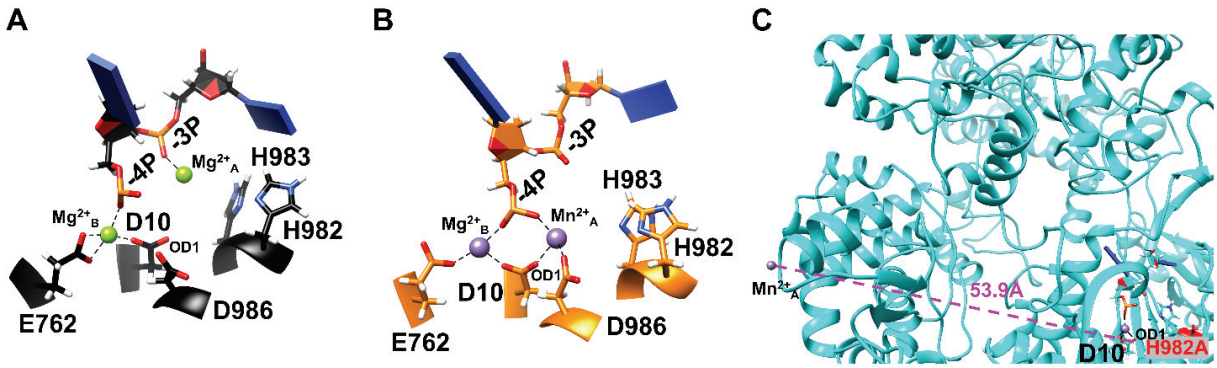

Figure S12. Detailed coordination of divalent metal ions and water molecules in the RuvC active sites of the different Cas9 proteins after ion perturbation analysis. Representative structures of **(A)** SpyCas9^{WT}+NTS-DNA+Mg^{2+}, **(B)** SpyCas9^{WT}+NTS-DNA+Mn^{2+}, and **(C)** SpyCas9^{H982A}+NTS-DNA+Mn^{2+}. In **(A),** the $Mg^{2+}{}_A$ interacts with the phosphate group of -3P NTS-DNA and five water molecules, but it has lost its interaction with D10. This will create a non-catalytic stage of RuvC. In **(B),** the $Mn^{2+}{}_A$ is recruited and well-coordinated with D10, D986, phosphate group of -4P NTS-DNA, and three water molecules in the RuvC catalytic center. The coordination between -3P and $Mn^{2+}{}_A$ is replaced by a new coordination between -4P and $Mn^{2+}{}_A$ in SpyCas9^{WT}-Mn^{2+}. This maintains a catalytically competent stage. In **(C)**, $Mn^{2+}A$ is away from the RuvC center of SpyCas9^{H982A}, disrupting the catalytic stage. The pink dashed-line shows the distance between $Mn^{2+}A$ and D10@OD1.

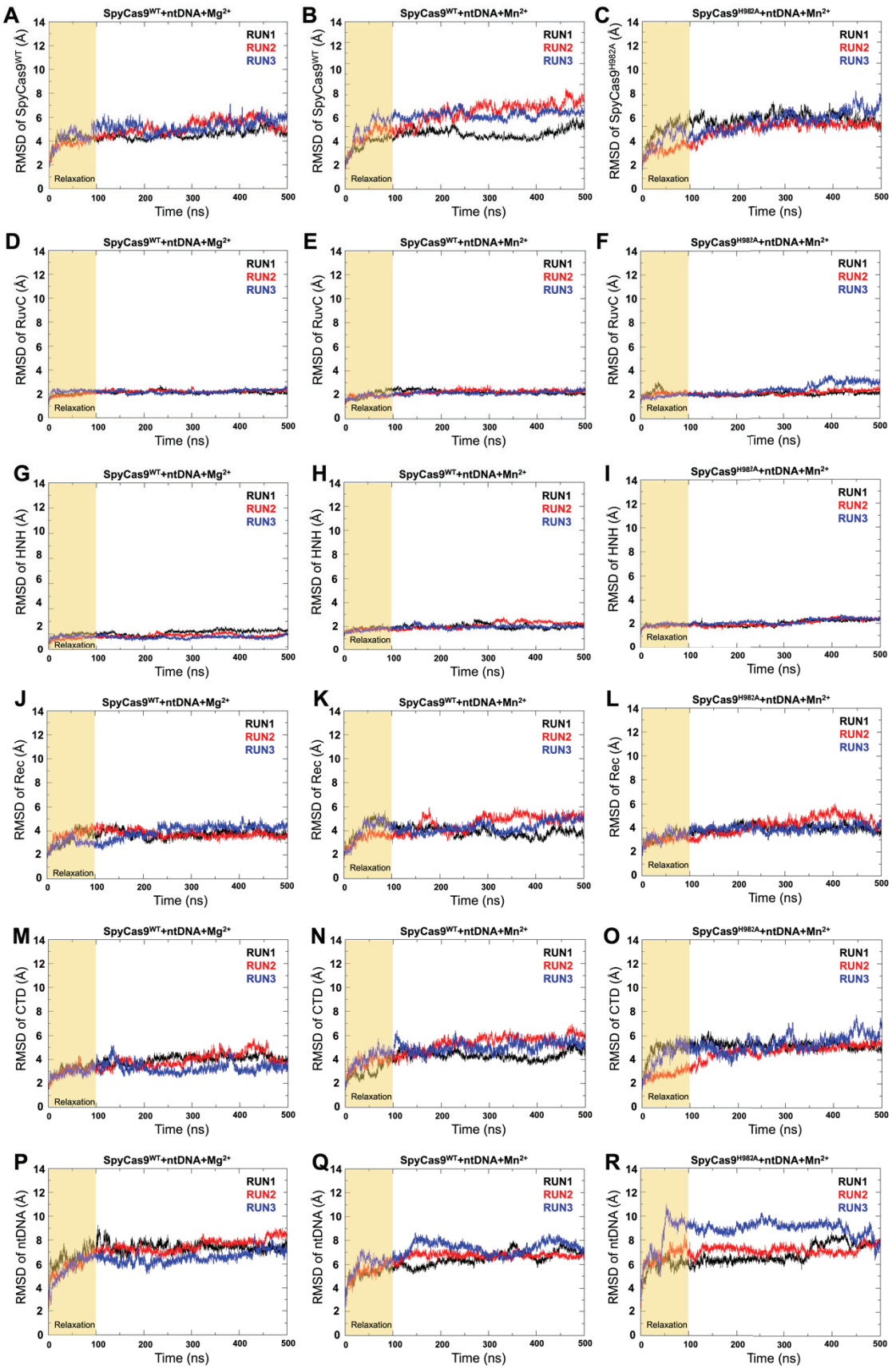
A
SpyCas9WT+ntDNA+Mg2+
RMSD of SpyCas9WT (Å)
B
SpyCas9WT+ntDNA+Mn2+
RMSD of SpyCas9WT (Å)
C
SpyCas9H982A+ntDNA+Mn2+
RMSD of SpyCas9H982A (Å)
D
SpyCas9WT+ntDNA+Mg2+
RMSD of RuvC (Å)
E
SpyCas9WT+ntDNA+Mn2+
RMSD of RuvC (Å)
F
SpyCas9H982A+ntDNA+Mn2+
RMSD of RuvC (Å)
G
SpyCas9WT+ntDNA+Mg2+
RMSD of HNH (Å)
H
SpyCas9WT+ntDNA+Mn2+
RMSD of HNH (Å)
I
SpyCas9H982A+ntDNA+Mn2+
RMSD of HNH (Å)
J
SpyCas9WT+ntDNA+Mg2+
RMSD of Rec (Å)
K
SpyCas9WT+ntDNA+Mn2+
RMSD of Rec (Å)
L
SpyCas9H982A+ntDNA+Mn2+
RMSD of Rec (Å)
M
SpyCas9WT+ntDNA+Mg2+
RMSD of CTD (Å)
N
SpyCas9WT+ntDNA+Mn2+
RMSD of CTD (Å)
O
SpyCas9H982A+ntDNA+Mn2+
RMSD of CTD (Å)
P
SpyCas9WT+ntDNA+Mg2+
RMSD of ntDNA (Å)
Q
SpyCas9WT+ntDNA+Mn2+
RMSD of ntDNA (Å)
R
SpyCas9H982A+ntDNA+Mn2+
RMSD of ntDNA (Å)
RUN1
RUN2
RUN3
Relaxation
Time (ns)

Figure S13. The histograms of mass-weighted atom RMSD in SpyCas9-NTS-DNA simulations for whole protein, different DNA domains, and NTS-DNA. A-C RMSD of the whole protein, **D-F** RMSD of the RuvC domain, **G-I** RMSD of the HNH domain, **J-L** RMSD of the recognition domain (REC), **M-O** RMSD of the C-terminal domain (CTD), and **P-R** RMSD of NTS-DNA. In each category, SpyCas9^{WT}+NTS-DNA+Mg^{2+}, SpyCas9^{WT}+NTS-DNA+Mn^{2+} and SpyCas9^{H982A}+NTS-DNA+Mn^{2+}, respectively, are shown. The RMSD analysis of individual run utilized the 500 ns MD production.

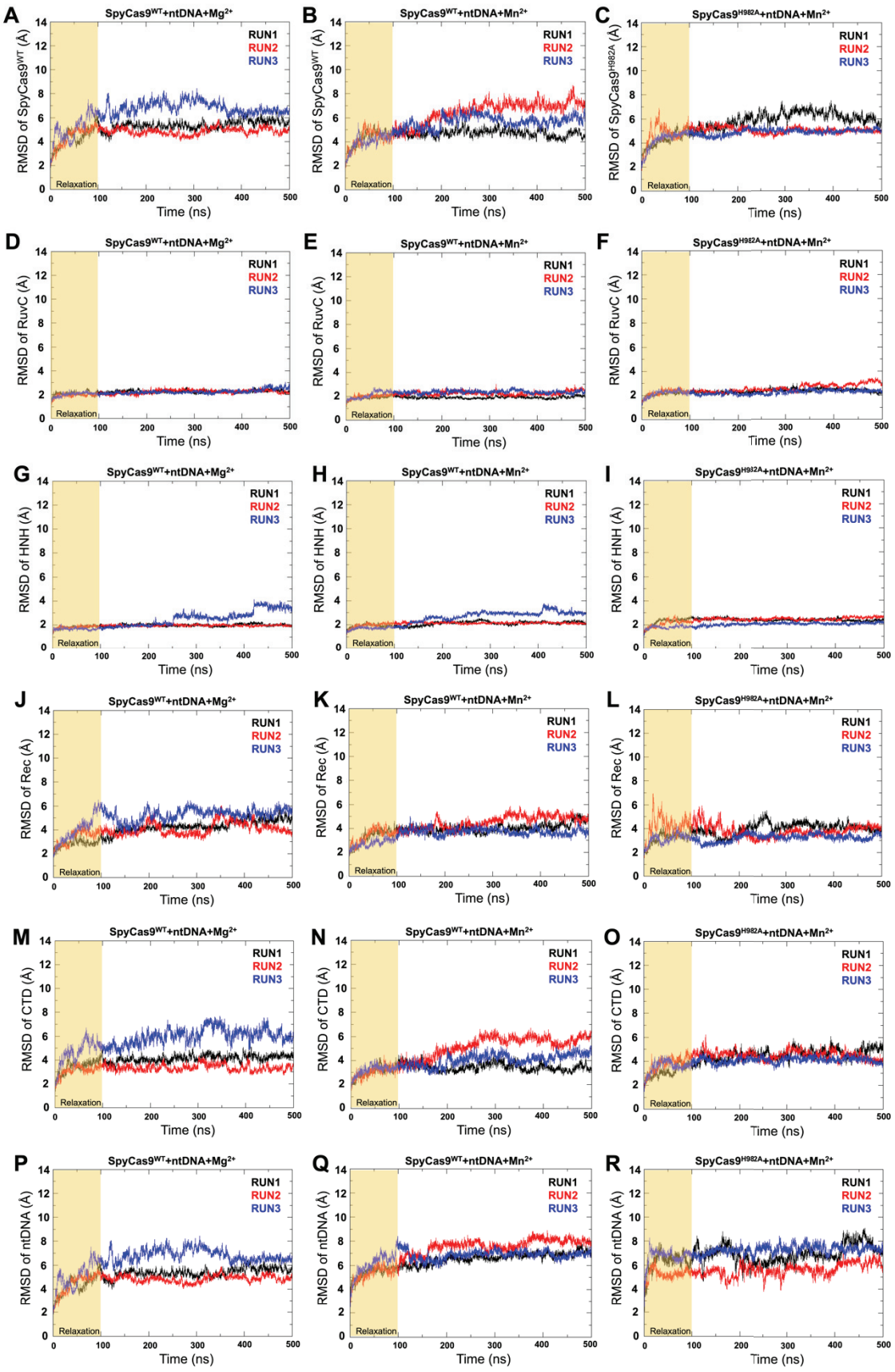
A
SpyCas9WT+ntDNA+Mg2+
RMSD of SpyCas9WT (Å)
B
SpyCas9WT+ntDNA+Mn2+
RMSD of SpyCas9WT (Å)
C
SpyCas9H982A+ntDNA+Mn2+
RMSD of SpyCas9H982A (Å)
D
SpyCas9WT+ntDNA+Mg2+
RMSD of RuvC (Å)
E
SpyCas9WT+ntDNA+Mn2+
RMSD of RuvC (Å)
F
SpyCas9H982A+ntDNA+Mn2+
RMSD of RuvC (Å)
G
SpyCas9WT+ntDNA+Mg2+
RMSD of HNH (Å)
H
SpyCas9WT+ntDNA+Mn2+
RMSD of HNH (Å)
I
SpyCas9H982A+ntDNA+Mn2+
RMSD of HNH (Å)
J
SpyCas9WT+ntDNA+Mg2+
RMSD of Rec (Å)
K
SpyCas9WT+ntDNA+Mn2+
RMSD of Rec (Å)
L
SpyCas9H982A+ntDNA+Mn2+
RMSD of Rec (Å)
M
SpyCas9WT+ntDNA+Mg2+
RMSD of CTD (Å)
N
SpyCas9WT+ntDNA+Mn2+
RMSD of CTD (Å)
O
SpyCas9H982A+ntDNA+Mn2+
RMSD of CTD (Å)
P
SpyCas9WT+ntDNA+Mg2+
RMSD of ntDNA (Å)
Q
SpyCas9WT+ntDNA+Mn2+
RMSD of ntDNA (Å)
R
SpyCas9H982A+ntDNA+Mn2+
RMSD of ntDNA (Å)
RUN1
RUN2
RUN3
Relaxation
Time (ns)

Figure S14. The histograms of mass-weighted heavy atom RMSD in SpyCas9-NTS-DNA simulations from ion-perturbation tests. A-C RMSD of the whole protein, **D-F** RMSD of the RuvC domain, **G-I** RMSD of the HNH domain, **J-L** RMSD of the recognition domain (REC), **M-O** RMSD of the C-terminal domain (CTD), and **P-R** RMSD of the NTS-DNA. In each category, SpyCas9^{WT}+NTS-DNA+Mg^{2+}, SpyCas9^{WT}+NTS-DNA+Mn^{2+} and SpyCas9^{H982A}+NTS-DNA+Mn^{2+}, respectively, are shown. The RMSD analysis of individual run utilizes 500 ns MD production.

Name	Purpose	Sequence
SpyCas9-H982A-FP	Forward PCR primer for SDM to introduce the H982A mutation into SpyCas9	TGAGATTAACAATTACGCTCATGCCCATGATGCGT
SpyCas9-H982A-RP	Reverse PCR primer for SDM to introduce the H982A mutation into SpyCas9	ACGCATCATGGGCATGAGCGTAATTGTTAATCTCA
sgRNA	*in vitro* DNA cleavage assays	*gaaattaatacgactcactata***GG**<u>**GATTTCTTCTTGCGCTTTTT**</u>GTTTT AGAGCTATGCTGTTTTG**gaaa**CAAAACAGCATAGCAAGTTAA AATAAGGCTAGTCCGTTATCAACTTGAAAAAGTGGCACCGA GTCGGTGCTT,TTTTAT<u>GTCTTC</u>- *italics* – T7 promoter <u>**BOLD UPPER CASE UNDERLINED**</u> – extra Gs for enhanced transcription **BOLD UPPER CASE** – 20 nt guide region bold lower case – tetra loop <u>underlined</u> – BbsI restriction sites comma (,) – the BbsI cut site
Matched (MCH) substrate	*in vitro* DNA cleavage assays	GATTTCTTCTTGCGCTTTTT
Mismatch in position 3 (MM3) substrate	*in vitro* DNA cleavage assays	GATTTCTTCTTGCGCTT**A**TT **Bold** - mismatch

Mismatch in position 5 (MM5) substrate	*in vitro* DNA cleavage assays	GATTTCTTCTTGCGC**A**TTTT **Bold** - mismatch
Mismatch in position 18 (MM18) substrate	*in vitro* DNA cleavage assays	GA**A**TTCTTCTTGCGCTTTTT **Bold** - mismatch
Matched target strand with 5' 6-FAM label	FAM-labeled DNA cleavage assay	CGACGGCCAGTGAATTCCCCAAAAAGCGCAAGAAGAAATCA ACCAGCGCAGGAT
Matched non-target strand with 5' 6-FAM label	FAM-labeled DNA cleavage assay	ATCCTGCGCTGGTTGATTTCTTCTTGCGCTTTTTGGGGAATT CACTGGCCGTCG

Table S1. Sequences of oligonucleotides used in this study (Shown in 5' to 3' direction)**.**

Named	Settings	Perturbations	Independent runs [time duration]
a	SpyCas9^{WT}+NTS-DNA+Mg^{2+}	None	S1, S2, S3 [500 ns]
b	SpyCas9^{WT}+NTS-DNA+Mn^{2+}	None	S1, S2, S3 [500 ns]
c	SpyCas9^{H982A}+NTS-DNA+Mn^{2+}	None	S1, S2, S3 [500 ns]
a-mv	SpyCas9^{WT}+NTS-DNA+Mg^{2+}	$Mg^{2+}{}_A$ moved away from D10	S1*, S2, S3 [500 ns]
b-mv	SpyCas9^{WT}+NTS-DNA+Mn^{2+}	$Mn^{2+}{}_A$ moved away from D10	S1, S2, S3* [500 ns]
c-mv	SpyCas9^{H982A}+NTS-DNA+Mn^{2+}	$Mn^{2+}{}_A$ moved away from D10	S1*, S2, S3 [500 ns]

Table S2. Summary of all MD simulations.

***** Served as representative simulations in Figure S12 A-C.

Analysis	Programs	Utilized settings (Based on Table S2)	Utilized trajectory	Time interval of extracted snapshots	Total extracted snapshots (Frames)
Contacts between SpyCas9 and NTS-DNA	CPPTRAJ	**a, b, c**	100-500 ns from all 3 individual runs	100 ps	4000*3 =12,000
Distance analysis	CPPTRAJ	**a, b, c; or a-mv, b-mv, c-mv**	100-500 ns from all 3 individual runs	100 ps	4000*3 =12,000
Free energy of binding between SpyCas9 and NTS-DNA	MM/GBSA	**a, b, c**	100-200 ns from all 3 individual runs	100 ps	1000*3 =3000
Free energy of binding between Mg^{2+}_A/Mg^{2+}_A and SpyCas9-NTS-DNA complex	MM/PBSA	**a-mv, b-mv, c-mv**	450-500 ns from the representative run (*-marked in Table S2)	2000 ps	250
mass-weighted heavy atom RMSD	CPPTRAJ	**a, b, c, a-mv, b-mv, c-mv**	1-500 ns from all 3 individual runs	100 ps	5000*3 =15,000

Table S3. The Summary of all computational analyses in this work.

	SpyCas9^{WT}+ntDNA+Mg^{2+} 451-500ns (250 frames)			SpyCas9^{WT}+ntDNA+Mn^{2+} 451-500ns (250 frames)		
Energy Component	Average	Std. Dev.	Std. Err. of Mean	Average	Std. Dev.	Std. Err. of Mean
VDWAALS	9.51404	2.555	0.36134	23.34602	4.5061	0.63726
EEL	-52.9842	20.76666	2.93686	**-171.36782**	27.07398	3.82884
EPB	79.80618	22.64464	3.20244	126.84966	22.59082	3.19482
ENPOLAR	-2.2403	0.08898	0.01258	-2.68414	0.05344	0.00756
EDISPER	1.89216	0.0837	0.01186	1.242	0.10798	0.01528
DELTA G gas	-43.47016	20.34632	2.87742	-148.0218	25.23454	3.5687
DELTA G solv	79.45804	22.60448	3.19676	125.40754	22.54642	3.18854
DELTA TOTAL	35.98784	10.76816	1.52284	-22.61426	7.81262	1.1049

VDWAALS = van der Waals contribution from molecular mechanics.
EEL = electrostatic energy as calculated by the molecular mechanics force field.
EPB/EGB = the electrostatic contribution to the solvation free energy calculated by PB or GB respectively.
ENPOLAR = nonpolar contribution to the solvation free energy calculated by an empirical model.
EDISPER= dispersion solvation free energy calculated by an empirical model.
DELTA G gas = estimated binding free energy in gas phase calculated from the terms above.
DELTA G solv = estimated binding free energy in solvent calculated from the terms above.
DELTA TOTAL = final estimated binding free energy calculated from the terms above.

Table S4. Estimated energy components from MM/PBSA calculation (all units in kcal/mol).

	SpyCas9^{WT}+NTS-DNA+Mg^{2+} 451-500ns (250 frames)			SpyCas9^{WT}+NTS-DNA+Mn^{2+} 451-500ns (250 frames)		
Residue	Avg.	Std. Dev.	Std. Err. of Mean	Avg.	Std. Dev.	Std. Err. of Mean
ASP 10	-5.198892	1.77439317	0.25093709	-32.21206	3.02771479	0.42818353
ASP 984	-3.025768	0.98275922	0.13898314	-27.497368	2.61535877	0.36986758
ntDNA -4P	-6.048852	1.16456439	0.16469428	-23.855984	3.59012373	0.50772017
ntDNA -3P	-23.988476	1.88819437	0.26703101	-4.692836	0.89526441	0.12660951

Table S5. Energy decomposition analysis (all units kcal/mol)

REFERENCES

1. Jinek M, Chylinski K, Fonfara I, et al. A Programmable Dual-RNA–Guided DNA Endonuclease in Adaptive Bacterial Immunity. Science 2012;337(6096):816-821, doi:10.1126/science.1225829
2. Sundaresan R, Parameshwaran HP, Yogesha SD, et al. RNA-Independent DNA Cleavage Activities of Cas9 and Cas12a. Cell Reports 2017;21(13):3728-3739, doi:10.1016/j.celrep.2017.11.100
3. Martin L, Rostami S, Rajan R. Optimized protocols for the characterization of Cas12a activities. Methods Enzymol 2023;679(97-129, doi:10.1016/bs.mie.2022.08.048
4. Case DA, Betz, R.M., Cerutti, D.S., Cheatham, III, T.E., Darden, T.A., Duke, R.E., Giese, T.J., Gohlke, H., Goetz, A.W., Homeyer, N., Izadi, S., Janowski, P., Kaus, J., Kovalenko, A., Lee, T.S., LeGrand, S., Li, P., Lin, C., Luchko, T., Luo, R., Madej, B., Mermelstein, D., Merz, K.M., Monard, G., Nguyen, H., Nguyen, H.T., Omelyan, I., Onufriev, A., Roe, D.R., Roitberg, A., Sagui, C., Simmerling, C.L., Botello-Smith, W.M., Swails, J., Walker, R.C., Wang, J., Wolf, R.M., Wu, X., Xiao, L., and Kollman, P.A. AMBER 2016. University of California, San Francisco 2016
5. Maier JA, Martinez C, Kasavajhala K, et al. ff14SB: Improving the Accuracy of Protein Side Chain and Backbone Parameters from ff99SB. J Chem Theory Comput 2015;11(8):3696-713, doi:10.1021/acs.jctc.5b00255
6. Galindo-Murillo R, Robertson JC, Zgarbova M, et al. Assessing the Current State of Amber Force Field Modifications for DNA. J Chem Theory Comput 2016;12(8):4114-27, doi:10.1021/acs.jctc.6b00186
7. Jorgensen WLC, J.; Madura, J. D.; Impey, R. W.; Klein, M. L. . Comparison of Simple Potential Functions for Simulating Liquid Water. J Chem Phys 1983;79(926−935, doi:https://doi.org/10.1063/1.445869
8. Joung IS, Cheatham TE, 3rd. Determination of alkali and halide monovalent ion parameters for use in explicitly solvated biomolecular simulations. J Phys Chem B 2008;112(30):9020-41, doi:10.1021/jp8001614
9. Li P, Roberts BP, Chakravorty DK, Merz KM, Jr. Rational Design of Particle Mesh Ewald Compatible Lennard-Jones Parameters for +2 Metal Cations in Explicit Solvent. J Chem Theory Comput 2013;9(6):2733-2748, doi:10.1021/ct400146w
10. Roe DR, Cheatham TE, 3rd. PTRAJ and CPPTRAJ: Software for Processing and Analysis of Molecular Dynamics Trajectory Data. J Chem Theory Comput 2013;9(7):3084-95, doi:10.1021/ct400341p
11. Babu K, Kathiresan V, Kumari P, et al. Coordinated Actions of Cas9 HNH and RuvC Nuclease Domains Are Regulated by the Bridge Helix and the Target DNA Sequence. Biochemistry 2021;60(49):3783-3800, doi:10.1021/acs.biochem.1c00354
12. Kollman SMPA. Settle: An analytical version of the SHAKE and RATTLE algorithm for rigid water models. Journal of Computational Chemistry 1992;13(8):952-962, doi:https://doi.org/10.1002/jcc.540130805
13. Feenstra KAH, B.; Berendsen, H. J. C. Improving Efficiency of Large Time-Scale Molecular Dynamics Simulations of Hydrogen-Rich Systems. J Comput Chem 1999;20(8):786-798
14. Hopkins CW, Le Grand S, Walker RC, Roitberg AE. Long-Time-Step Molecular Dynamics through Hydrogen Mass Repartitioning. J Chem Theory Comput 2015;11(4):1864-74, doi:10.1021/ct5010406
15. Salomon-Ferrer R CD, Walker RC. . An overview of the amber biomolecular simulation package. Wiley Interdisciplinary Reviews: Computational Molecular Science 2013;3(2):198-210, doi:DOI: https://doi.org/10.1002/ wcms.1121

16. Miller BR, 3rd, McGee TD, Jr., Swails JM, et al. MMPBSA.py: An Efficient Program for End-State Free Energy Calculations. J Chem Theory Comput 2012;8(9):3314-21, doi:10.1021/ct300418h
17. Hou T, Wang J, Li Y, Wang W. Assessing the performance of the MM/PBSA and MM/GBSA methods. 1. The accuracy of binding free energy calculations based on molecular dynamics simulations. J Chem Inf Model 2011;51(1):69-82, doi:10.1021/ci100275a
18. Genheden S, Ryde U. The MM/PBSA and MM/GBSA methods to estimate ligand-binding affinities. Expert Opin Drug Discov 2015;10(5):449-61, doi:10.1517/17460441.2015.1032936
19. Turner P. XMGRACE, Version 5.1. 19. Center for Coastal and Land-Margin Research, Oregon Graduate Institute of Science and Technology, Beaverton, OR 2005;2
20. Jinek M, Jiang F, Taylor DW, et al. Structures of Cas9 endonucleases reveal RNA-mediated conformational activation. Science 2014;343(6176):1247997, doi:10.1126/science.1247997

UNCROPPED GELS AND REPLICATIONS

Figure 1. Divalent metal dependence of gRNA-free DNA cleavage.

WT, 1 mM
R1

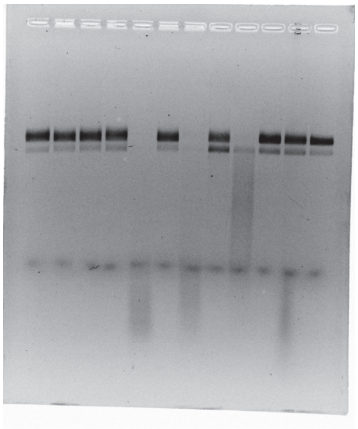

Lane order:
Control (no protein), Control (no metal), EDTA, Mg^{2+}, Mn^{2+}, Ca^{2+}, Co^{2+}, Ni^{2+}, Cu^{2+}, Zn^{2+}, Cd^{2+}, Ba^{2+}

R2

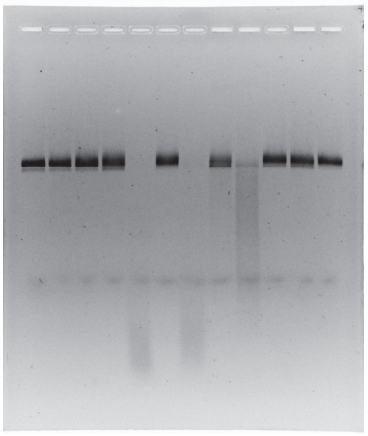

Lane order:
Control (no protein), Control (no metal), EDTA, Mg^{2+}, Mn^{2+}, Ca^{2+}, Co^{2+}, Ni^{2+}, Cu^{2+}, Zn^{2+}, Cd^{2+}, Ba^{2+}

R3

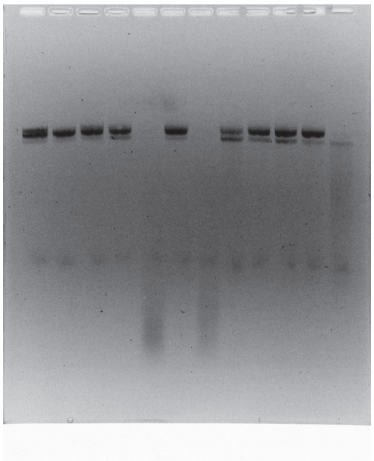

Lane order:
Control (no protein), Control (no metal), EDTA, Mg^{2+}, Mn^{2+}, Ca^{2+}, Co^{2+}, Ni^{2+}, Zn^{2+}, Cd^{2+}, Ba^{2+}, Cu^{2+}

WT, 10 mM

R1

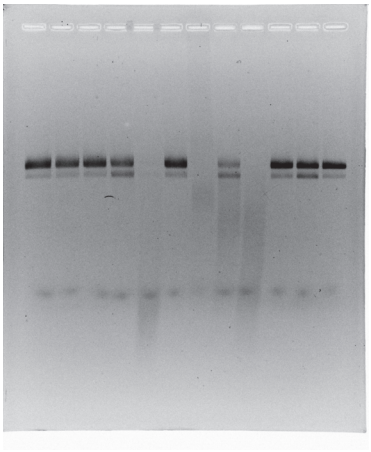

Lane order:
Control (no protein), Control (no metal), EDTA, Mg^{2+}, Mn^{2+}, Ca^{2+}, Co^{2+}, Ni^{2+}, Cu^{2+}, Zn^{2+}, Cd^{2+}, Ba^{2+}

R2

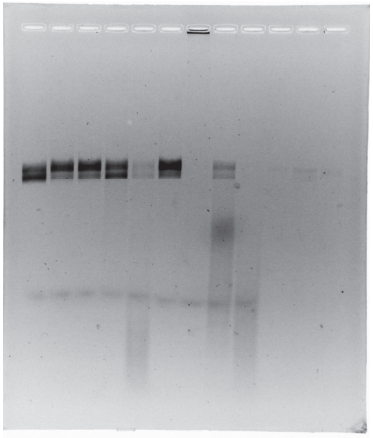

Lane order:
Control (no protein), Control (no metal), EDTA, Mg^{2+}, Mn^{2+}, Ca^{2+}, Co^{2+}, Ni^{2+}, (lanes 9-12 were not used for quantification)

R3

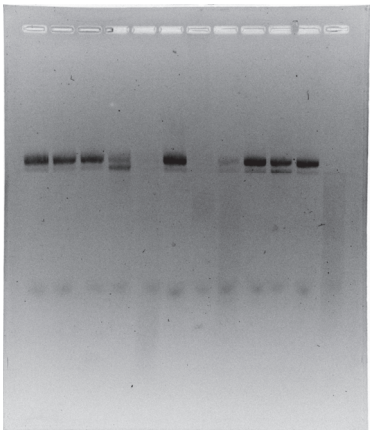

Lane order:
Control (no protein), Control (no metal), EDTA, Mg^{2+}, Mn^{2+}, Ca^{2+}, Co^{2+}, Ni^{2+}, Zn^{2+}, Cd^{2+}, Ba^{2+}, Cu^{2+}

H982A, 1 mM
R1

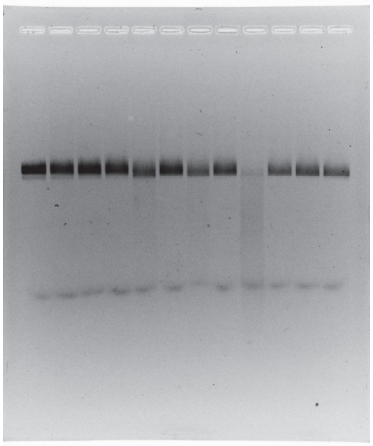

Lane order:
Control (no protein), Control (no metal), EDTA, Mg^{2+}, Mn^{2+}, Ca^{2+}, Co^{2+}, Ni^{2+}, Cu^{2+}, Zn^{2+}, Cd^{2+}, Ba^{2+}

R2

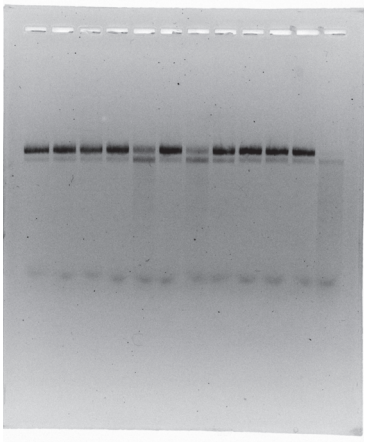

Lane order:
Control (no protein), Control (no metal), EDTA, Mg^{2+}, Mn^{2+}, Ca^{2+}, Co^{2+}, Ni^{2+}, Zn^{2+}, Cd^{2+}, Ba^{2+}, Cu^{2+}

R3

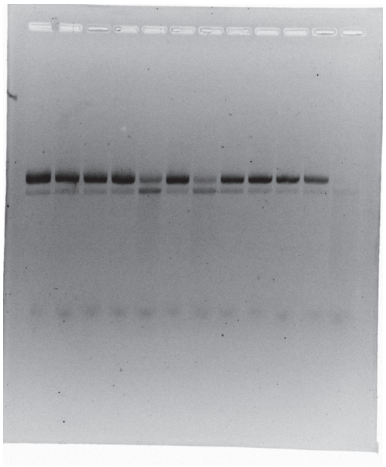

Lane order:
Control (no protein), Control (no metal), EDTA, Mg^{2+}, Mn^{2+}, Ca^{2+}, Co^{2+}, Ni^{2+}, Zn^{2+}, Cd^{2+}, Ba^{2+}, Cu^{2+}

H982A, 10 mM
R1

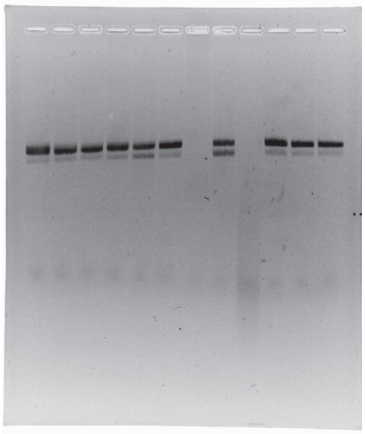

Lane order:
Control (no protein), Control (no metal), EDTA, Mg^{2+}, Mn^{2+}, Ca^{2+}, Co^{2+}, Ni^{2+}, Cu^{2+}, Zn^{2+}, Cd^{2+}, Ba^{2+}

R2

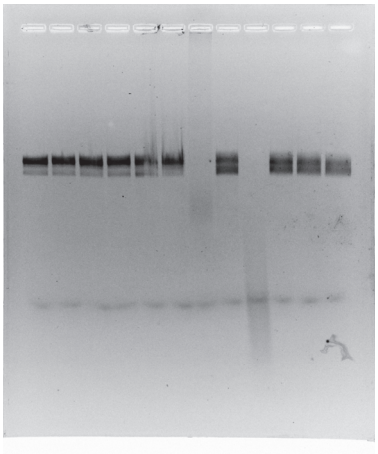

Lane order:
Control (no protein), Control (no metal), EDTA, Mg^{2+}, Mn^{2+}, Ca^{2+}, Co^{2+}, Ni^{2+}, Cu^{2+}, Zn^{2+}, Cd^{2+}, Ba^{2+}

R3

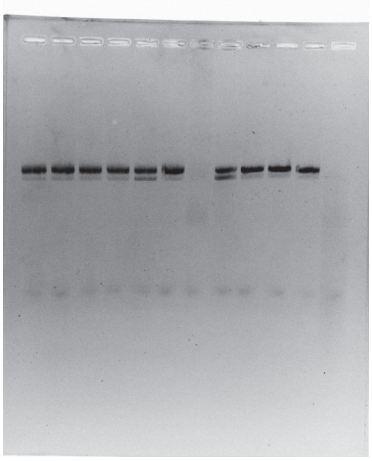

Lane order:
Control (no protein), Control (no metal), EDTA, Mg^{2+}, Mn^{2+}, Ca^{2+}, Co^{2+}, Ni^{2+}, Zn^{2+}, Cd^{2+}, Ba^{2+}, Cu^{2+}

Figure 2. Rate constants (k_{obs}, min^{-1}) and representative gels for gRNA-free cleavage of single stranded M13mp18 DNA with Mn^{2+}.

Mn^{2+}, WT

R1

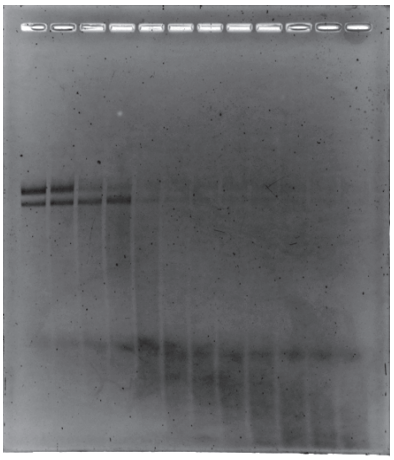

R2

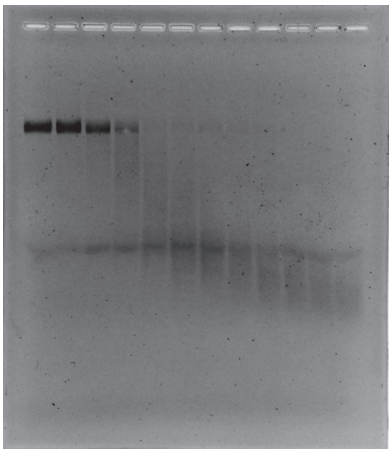

R3

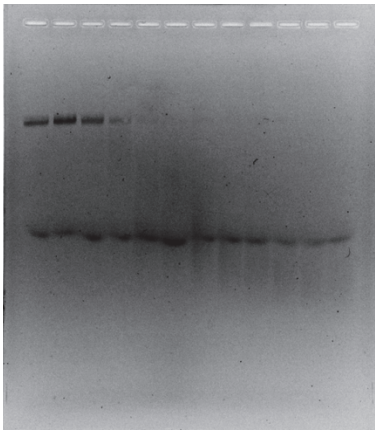

Mn^{2+}, H982A

R1

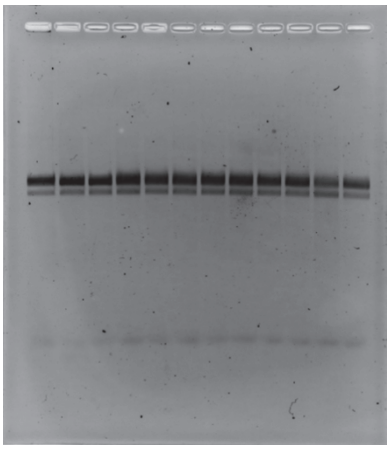

R2

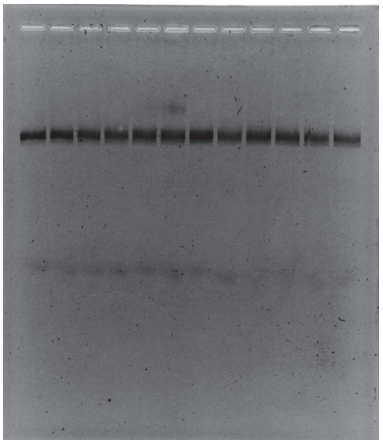

R3

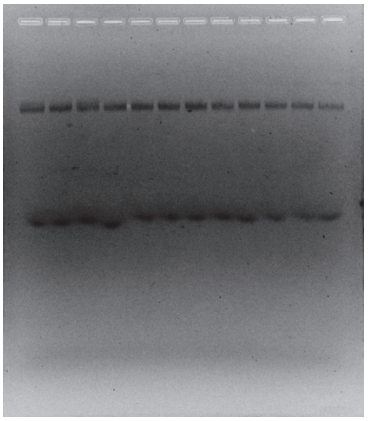

Order of loading same as Figure 2 of main text.

Figure 3. Assessment of gRNA-dependent DNA cleavage at 37°C with Mg^{2+} (with preincubation).

Mg^{2+}, WT

R1 R2 R3

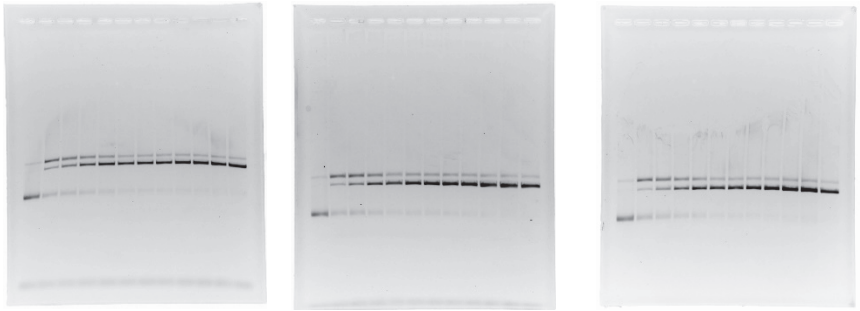

Mg^{2+}, H982A

R1 R2 R3

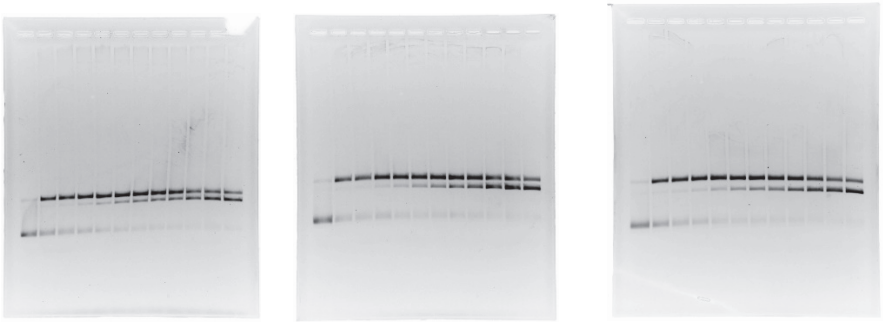

Order of loading same as Figure 3 of main text.

Figure 4. Mismatched DNA substrate cleavage assay to assess on-target selectivity (off-target discrimination.

R1

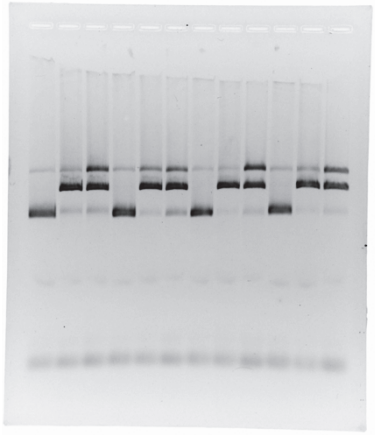

R2

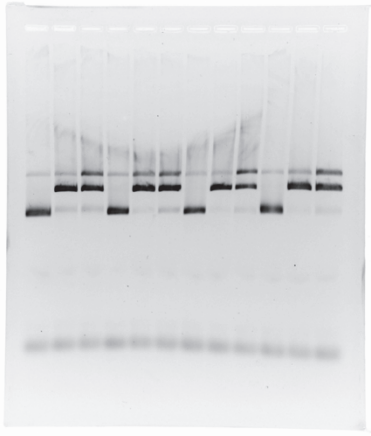

R3

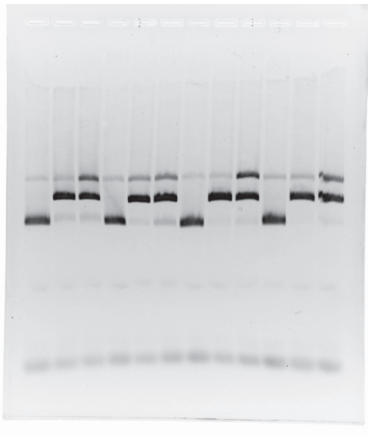

Order of loading same as Figure 4 of main text.

Figure S2. Characterizing different RuvC active site variants of SpyCas9 for their ability to promote gRNA-free DNA cleavage.

Panel A

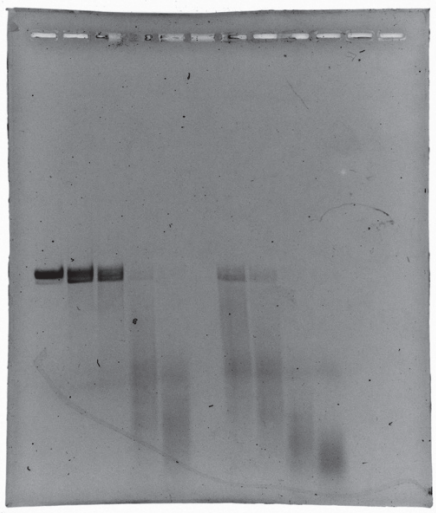

Panel C

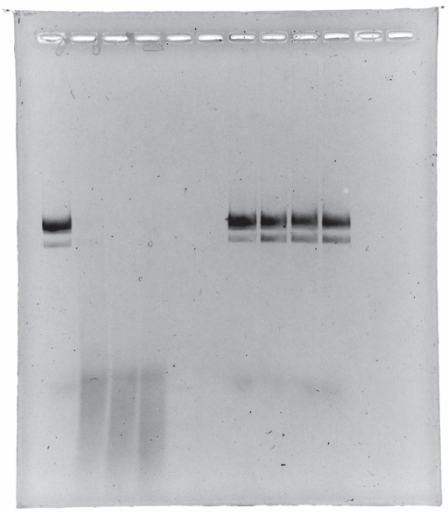

Panel B

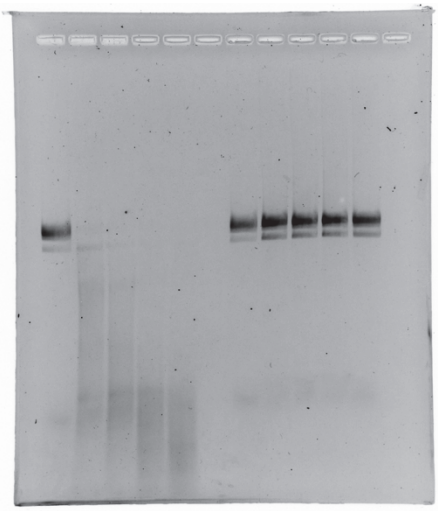

Panel D

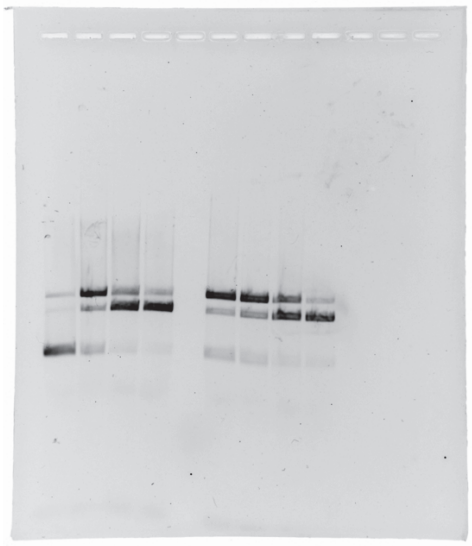

Order of loading same as Figure S2.

Panel E

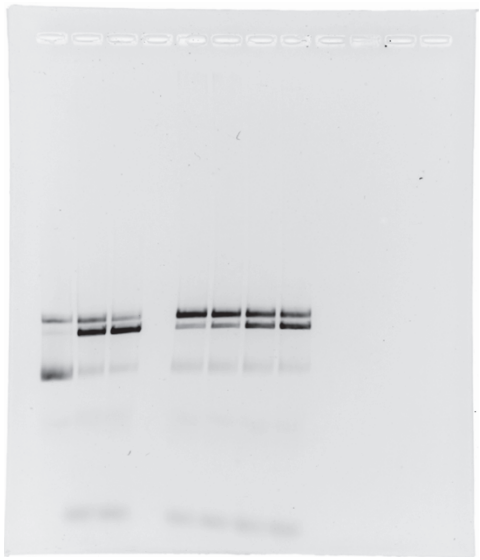

Panel G

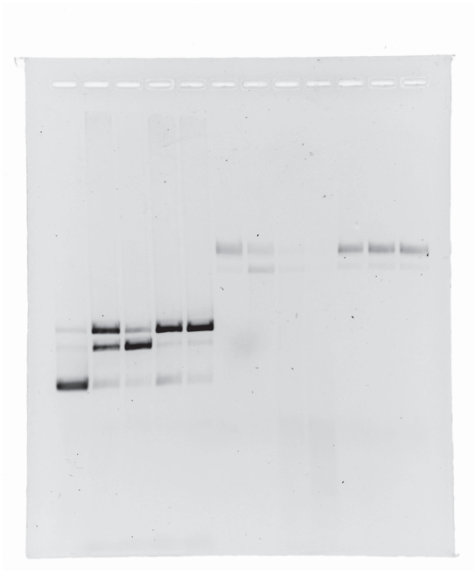

Panel F

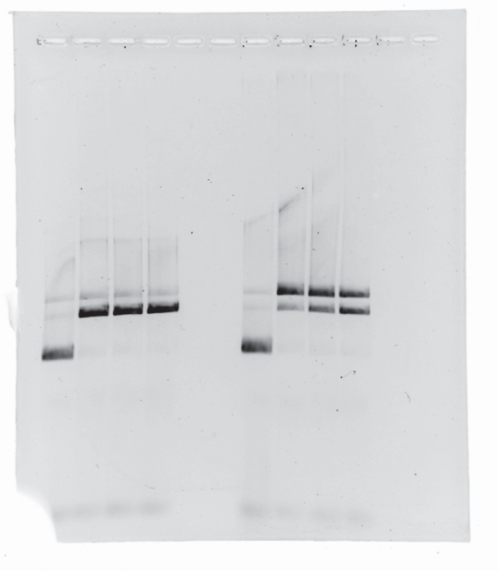

Order of loading same as Figure S2.

Figure S3. SpyCas9 protein concentration titration assay of gRNA-free ssDNA cleavage with Mn^{2+}.

R1

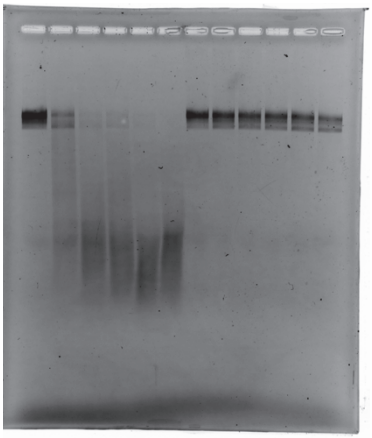

R2

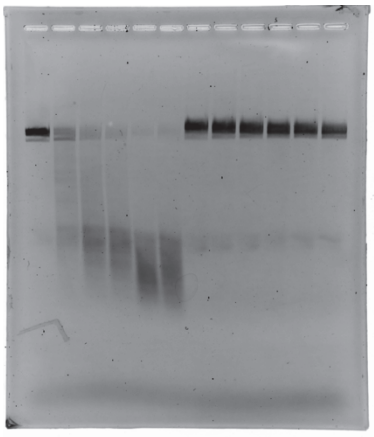

R3

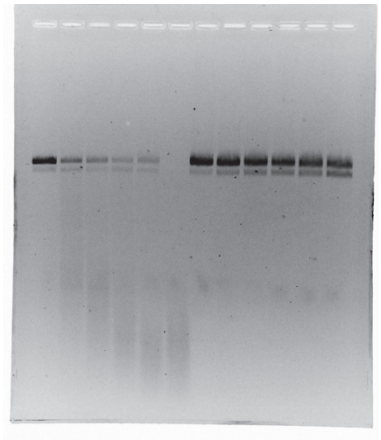

Order of loading same as Figure S3.

Figure S4. Analysis of the effect of different divalent metals on gRNA-free DNA cleavage.

Gels are same as in Figure 1.

Figure S5. Divalent metal titration assay of SpyCas9 gRNA-free ssDNA cleavage.

WT, Mn^{2+}
R1

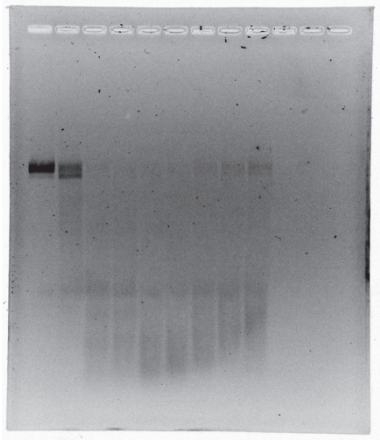

R2

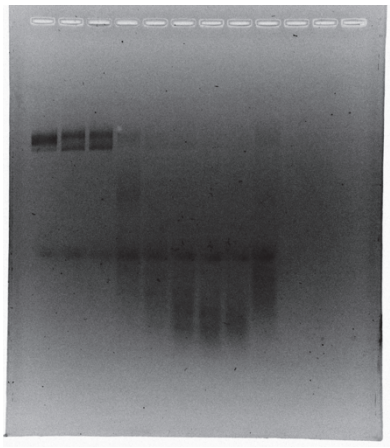

R3

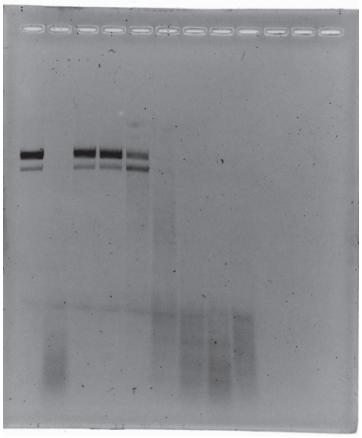

H982A, Mn^{2+}
R1

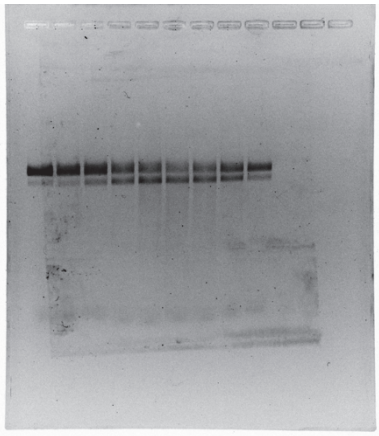

R2

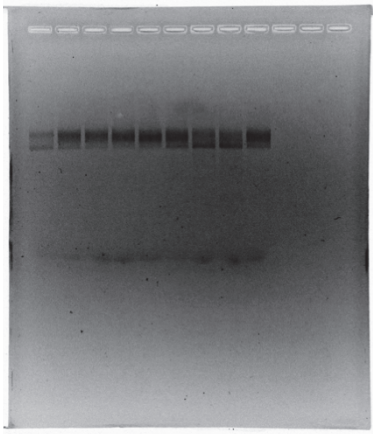

R3

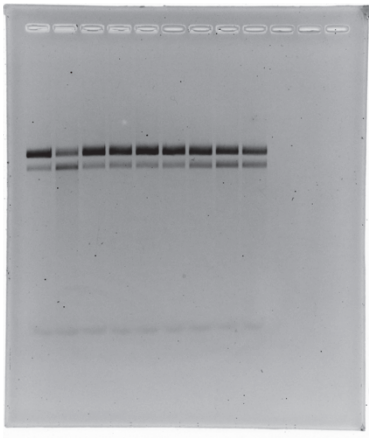

Order of loading same as Figure S5, except in R3 where 10 μM and 10 mM lanes got switched

WT, Co^{2+}
R1

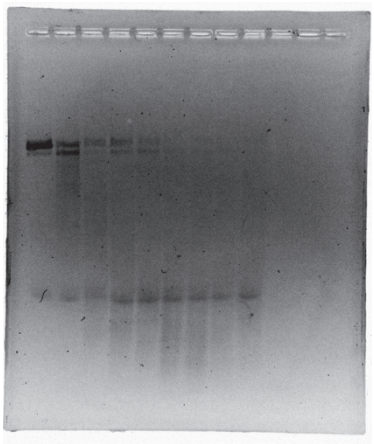

R2

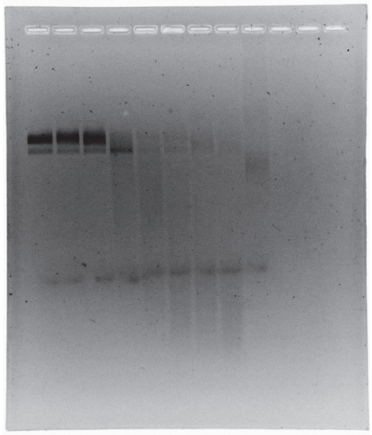

R3

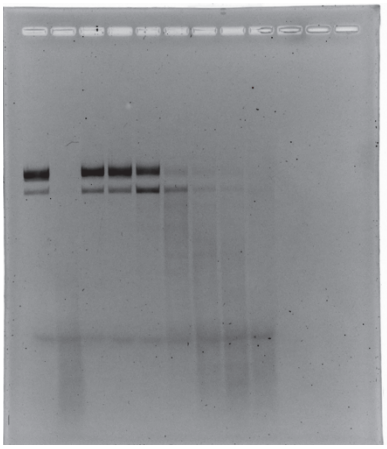

H982A, Co^{2+}
R1

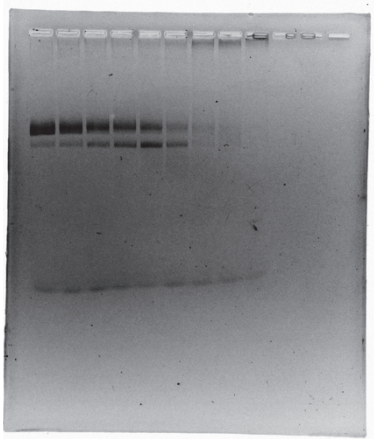

R2

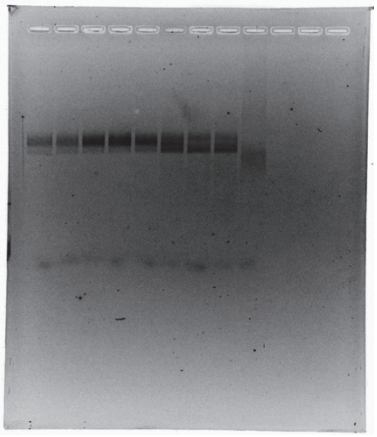

R3

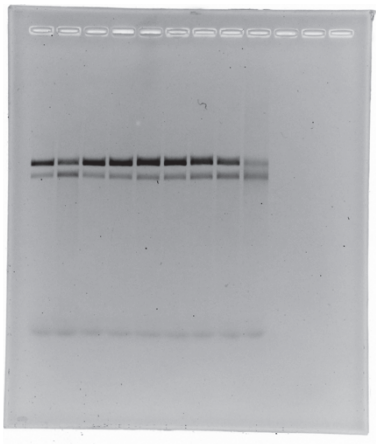

Order of loading same as Figure S5, except in R3 where 10 μM and 10 mM lanes got switched.

Figure S6. Determination of rate constant for SpyCas9 gRNA-free cleavage of circular, single stranded M13mp18 DNA in the presence of Co^{2+}.

Co^{2+}, WT

R1

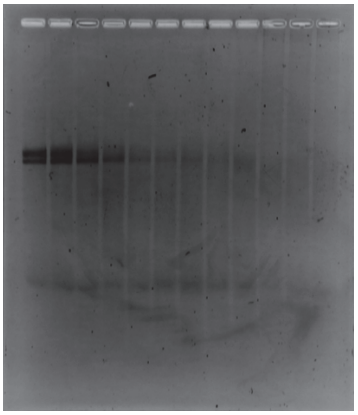

R2

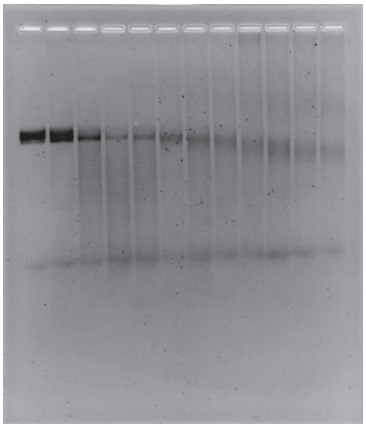

R3

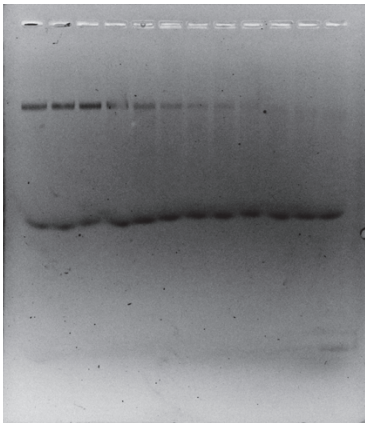

Co^{2+}, H982A

R1

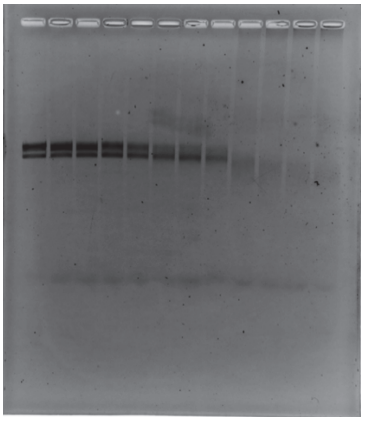

R2

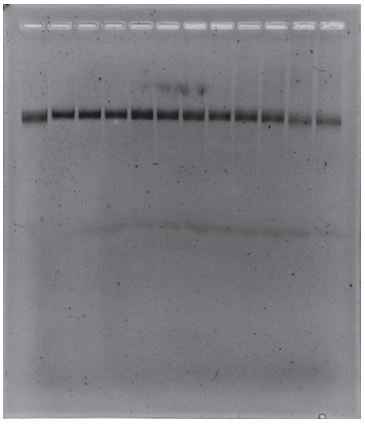

R3

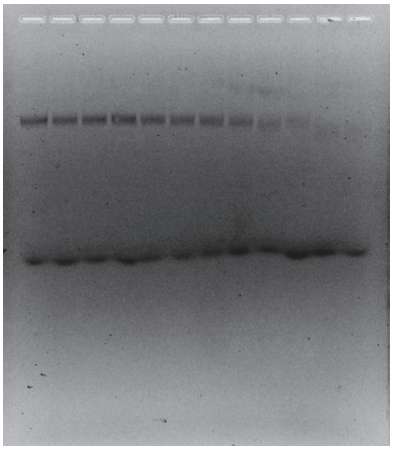

Order of loading same as Figure S6.

Figure S7. Assessment of gRNA-dependent DNA cleavage at 37°C without pre-incubation of Cas9 and gRNA to form the binary complex in the presence of Mg^{2+}.

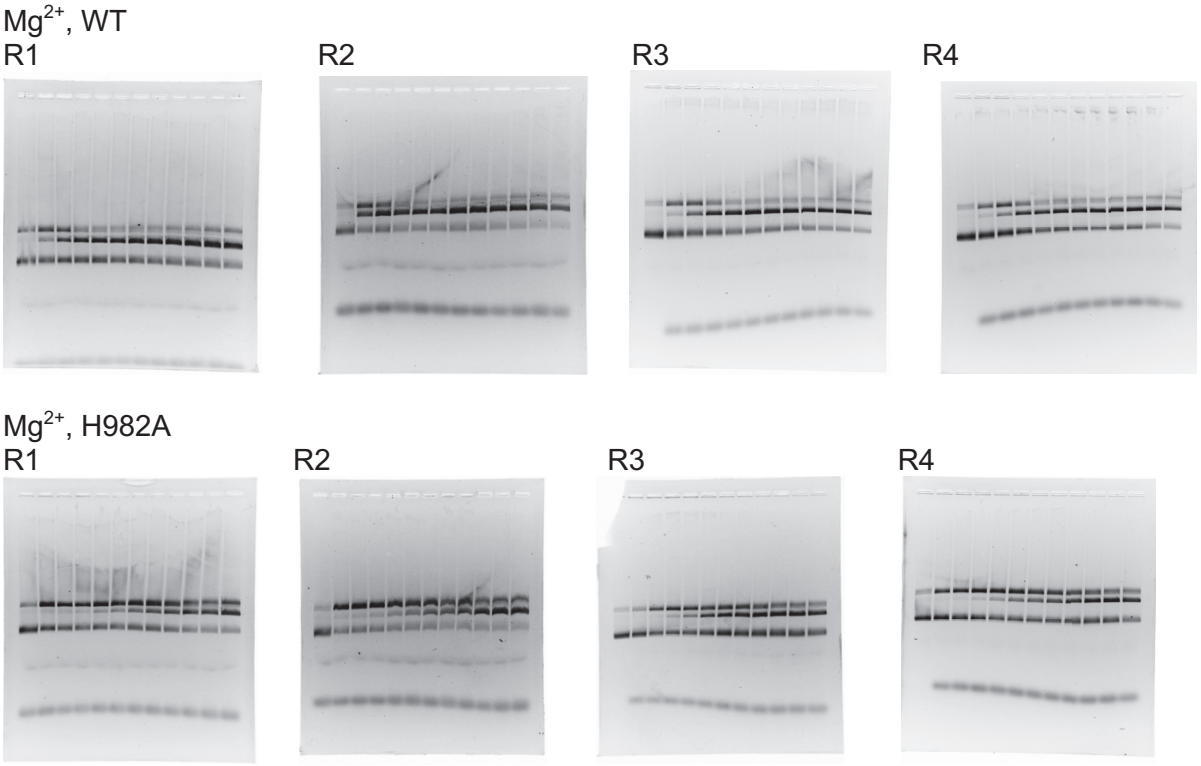

Figure S8. Assessment of TS cleavage by HNH using DNA oligo substrates.

WT, TS Cleavage, Mg^{2+}
R1

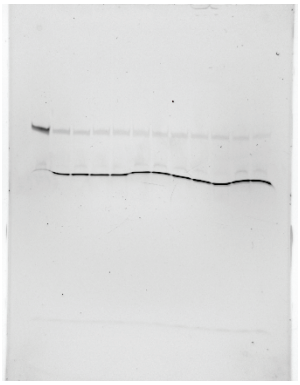

R2

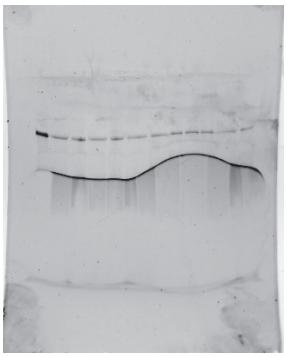

R3

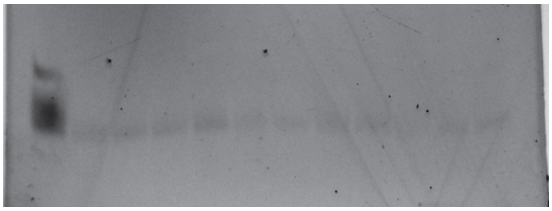

H982A, TS Cleavage, Mg^{2+}

R1

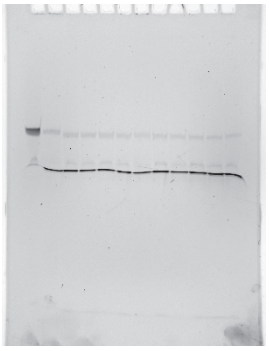

R2

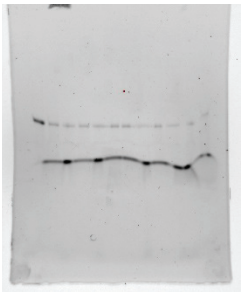

R3

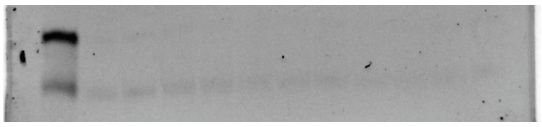

Figure S9. Assessment of NTS cleavage by RuvC using DNA oligo substrates.

WT, NTS Cleavage, Mg^{2+}
R1

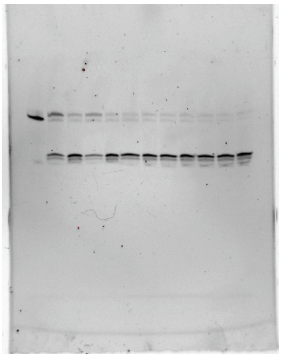

R2

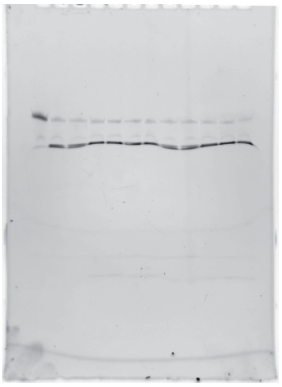

R3

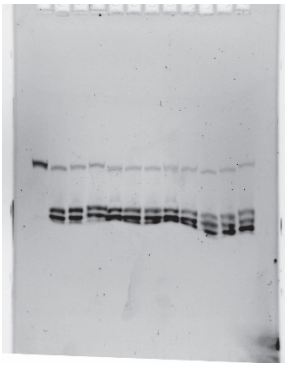

H982A, NTS Cleavage, Mg^{2+}

R1

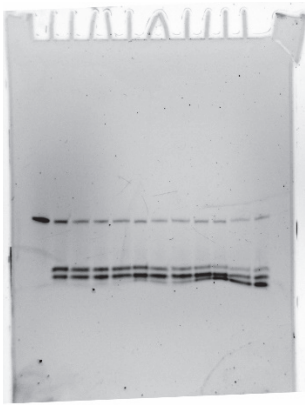

R2

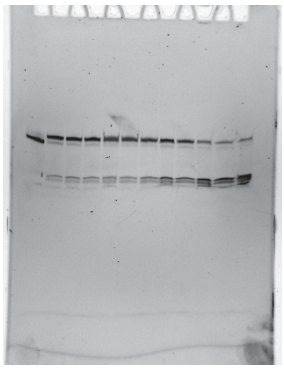

R3